



**HAL**  
open science

## Mesoscale SST – Wind Stress coupling in the Peru–Chile Current System: Which mechanisms drive its seasonal variability?

Véra Oerder, François Colas, Vincent Echevin, Sébastien Masson, Christophe Hourdin, Swen Jullien, Gurvan Madec, Florian Lemarié

### ► To cite this version:

Véra Oerder, François Colas, Vincent Echevin, Sébastien Masson, Christophe Hourdin, et al.. Mesoscale SST – Wind Stress coupling in the Peru–Chile Current System: Which mechanisms drive its seasonal variability?. *Climate Dynamics*, 2016, 47 (7), pp.2309-2330. 10.1007/s00382-015-2965-7. hal-01253181

**HAL Id: hal-01253181**

**<https://inria.hal.science/hal-01253181>**

Submitted on 25 Mar 2016

**HAL** is a multi-disciplinary open access archive for the deposit and dissemination of scientific research documents, whether they are published or not. The documents may come from teaching and research institutions in France or abroad, or from public or private research centers.

L'archive ouverte pluridisciplinaire **HAL**, est destinée au dépôt et à la diffusion de documents scientifiques de niveau recherche, publiés ou non, émanant des établissements d'enseignement et de recherche français ou étrangers, des laboratoires publics ou privés.

[Click here to view linked References](#)

<b>Climate Dynamics manuscript No.</b> (will be inserted by the editor)
--

---

1 **Mesoscale SST - Wind Stress coupling in the Peru-Chile Current System**

2 **which mechanisms drive its seasonal variability ?**

3 **Vera Oerder · François Colas · Vincent Echevin ·**

4 **Sebastien Masson · Christophe Hourdin · Swen Jullien ·**

5 **Gurvan Madec · Florian Lemarié**

6 Received: date / Accepted: date

---

V. Oerder  
LOCEAN-IPSL, CNRS/IRD/UPMC, UMR7159, Paris, France  
Tel.: +33 (1) 44 27 27 11  
E-mail: vera.oerder@locean-ipsl.upmc.fr

F. Colas  
LOCEAN-IPSL, CNRS/IRD/UPMC, UMR7159, Paris, France

V. Echevin  
LOCEAN-IPSL, CNRS/IRD/UPMC, UMR7159, Paris, France

S. Masson  
LOCEAN-IPSL, CNRS/IRD/UPMC, UMR7159, Paris, France

C. Hourdin  
LOCEAN-IPSL, CNRS/IRD/UPMC, UMR7159, Paris, France

S. Jullien  
LOS, IFREMER, Plouzané, France

F. Lemarié  
INRIA, Univ. Grenoble Alpes, CNRS, LJK, F-38000, Grenoble, France

G. Madec  
LOCEAN-IPSL, CNRS/IRD/UPMC, UMR7159, Paris, France

7 **Abstract** Satellite observations and a high-resolution regional ocean-atmosphere coupled model are used to  
8 study the air/sea interactions at the oceanic mesoscale in the Peru-Chile upwelling current system. Coupling  
9 between mesoscale Sea Surface Temperature (SST) and Wind Stress (WS) intensity is evidenced and character-  
10 ized by correlations and regression coefficients. Both the model and the observations display similar spatial and  
11 seasonal variability of the coupling characteristics that are stronger off Peru than off Northern Chile, in relation  
12 with stronger wind mean speed and steadiness. The coupling is also more intense during winter than during  
13 summer in both regions. It is shown that WS intensity anomalies due to SST anomalies are mainly forced by  
14 mixing coefficient anomalies and partially compensated by wind shear anomalies. A momentum balance analysis  
15 shows that wind speed anomalies are created by stress shear anomalies. Near-surface pressure gradient anomalies  
16 have a negligible contribution because of the back-pressure effect related to the air temperature inversion. As  
17 mixing coefficients are mainly unchanged between summer and winter, the stronger coupling in winter is due to  
18 the enhanced large-scale wind shear that enables a more efficient action of the turbulent stress perturbations.  
19 This mechanism is robust as it does not depend on the choice of planetary boundary layer parameterization.

20 **Keywords** ocean-atmosphere interactions · mesoscale SST-wind stress coupling · regional coupled modeling ·  
21 Eastern Boundary Upwelling System

## 22 1 Introduction

23 Surface Wind Stress (WS) is one of the main forcing of the ocean dynamics. Coarse spatial resolution sea surface  
 24 temperature (SST) and WS intensity fields present negative correlations (Liu et al, 1994; Xie, 2004), charac-  
 25 teristic of an ocean driven by the atmosphere : more intense WS cools the surface water through evaporation  
 26 and entrainment of subsurface water in the mixed layer. However, higher resolution fields contain mesoscale  
 27 structures ( $\sim 10$  to  $100$  km, scales corresponding to the oceanic mesoscale) that show a contrasting behavior.  
 28 SST-WS intensity correlations are positive under the effect of the ocean feedback on the atmosphere (Small  
 29 et al, 2008). The atmospheric response to the SST was first observed by Sweet et al (1981) above the north wall  
 30 of the Gulf Stream. A cross-front WS intensity increase was detected when passing from cold to warm waters.  
 31 Further observational campaigns (Businger and Shaw, 1984; Giordani et al, 1998) in other regions also evidenced  
 32 enhanced (weakened) WS intensity over warmer (colder, respectively) SST. Then, satellite data confirmed this  
 33 result (Chelton et al, 2001; Bourras et al, 2004) and a proportional relationship between WS intensity and SST  
 34 mesoscale anomalies has been identified (*e.g.* O'Neill et al, 2010) :

$$\|\vec{\tau}_s\|' \propto SST' \quad (1)$$

35 with  $'$  the mesoscale anomalies, and  $\vec{\tau}_s$  the WS. The spatial derivative of relation (1) leads to relations between  
 36 the WS divergence (curl, respectively) and the downwind (crosswind) SST gradients. Theses relations and  
 37 relation (1) have been verified in several regions both with observations (*e.g.* O'Neill et al, 2005; Chelton et al,  
 38 2007; Castelao, 2012; Frenger et al, 2013) and models (*e.g.* Maloney and Chelton, 2006; Bryan et al, 2010;  
 39 O'Neill et al, 2010). A concurrent relation between SST laplacian and the near-surface wind speed divergence  
 40 has been proposed by Minobe et al (2008), assuming the surface wind speed to be proportional to the WS. In  
 41 this case, the WS divergence is proportional to the SST Laplacian (and not to the downwind SST gradient). In  
 42 the present work we focus on relation (1) because it shows the strongest correlations in our region of interest.  
 43 A comparison between the two types of SST-WS interactions is presented in the discussion (Sec. 5.3).

44 As recently underlined by Byrne et al (2015), the mechanisms leading to SST and WS intensity correlated  
45 patterns remain unclear and various processes have been proposed to explain (1). In the atmospheric Planetary  
46 Boundary Layer (PBL), the turbulent vertical mixing of momentum can be parameterized by a turbulent stress  
47  $\vec{\tau}$ . WS is the boundary condition of the turbulent stress at the air/sea interface. Samelson et al (2006) relate  
48 WS to the turbulent stress vertical shear and the PBL height, defined as the height above which  $\vec{\tau}$  vanishes.  
49 Under the strong assumption of an unchanged vertical stress shear, a PBL height increase above warm waters  
50 would result in a WS intensity increase. SST mesoscale anomalies could also affect the pressure in the PBL  
51 (Lindzen and Nigam, 1987, hereafter LN87), resulting in WS modifications through the momentum balance  
52 (Wai and Stage, 1989; Small et al, 2005). Finally, warm mesoscale anomalies could also enhance the mixing in  
53 the PBL. This would increase the transfer of momentum from the upper layers to the ocean surface, resulting  
54 in wind speed and stress strengthening in the lower layers (“downward mixing mechanism”; Hayes et al, 1989;  
55 Wallace et al, 1989). These mechanisms have also been shown to act together to explain the proportional relation  
56 between SST and WS intensity anomalies (O’Neill et al, 2010; Koseki and Watanabe, 2010). Byrne et al (2015)  
57 also pointed out a lack of explanation for the seasonal variability in the atmospheric response to the mesoscale  
58 SST.

59 Impacts of these mesoscale SST-WS interactions on the atmosphere and ocean dynamics at larger scale  
60 remain relatively unknown. In an idealized framework, Hogg et al (2009) showed that it can affect the large-  
61 scale ocean circulation and the gyres structure. Piazza et al (2015) recently showed that the mesoscale SST  
62 forcing in the Gulf Stream region have an upscaling impact on the tropospheric wind and storm tracks from  
63 the North American East Coast to the Mediterranean Sea. In Eastern Boundary Upwelling Systems (EBUS),  
64 WS can be significantly altered by the SST in offshore regions (Chelton et al, 2007) and also in coastal areas  
65 with strong thermal gradients due to the upwelling. In the California EBUS, Boe et al (2011) and Renault et al  
66 (2015) have shown that the nearshore wind shape is mainly driven by orographic effects, but the coupling with  
67 the SST, albeit weaker, can also modulate the nearshore WS structure. This WS modulation could affect in  
68 return the upwelling structure (Perlin et al, 2007; Jin et al, 2009), the associated coastal current system and  
69 also the eddy dynamics generated by its instability (*e.g.* Capet et al, 2008; Colas et al, 2012). The SST-WS

70 feedback could also affect the ocean mesoscale eddies characteristics, for example through Ekman pumping (*e.g.*  
71 Spall, 2007a; Gaube et al, 2015) created by WS mesoscale anomalies. In the EBUS mesoscale eddies play an  
72 important role as they can account for a substantial heat transport (Colas et al, 2012) and they also largely  
73 influence the intense biological activity (Lathuilière et al, 2010; Gruber et al, 2011; Bertrand et al, 2014).

74 The Peru-Chile Current System (PCS) is one of the main EBUS. Its regional dynamics has often been studied  
75 using regional ocean models forced by prescribed atmospheric fluxes (*e.g.* Penven et al, 2005; Oerder et al, 2015)  
76 neglecting the ocean feedback on the atmosphere. Recent advances in regional modeling now allow to tackle  
77 ocean/atmosphere mesoscale coupling in a realistic framework with the objective to understand its impact on  
78 the regional dynamics. The present study analyzes the characteristics of the SST feedback on the WS in the  
79 PCS. It also aims at understanding the mechanisms of the WS intensity response to SST in order to explain  
80 its seasonal variations. Putrasahan et al (2013) used an ocean/atmosphere coupled model to study the PCS  
81 dynamics. They concluded to a weak mesoscale air-sea coupling. However our study shows contrasting results.

82 In the present work, we use satellite observations and a high-resolution coupled model. Details about the  
83 model and observations are provided in section 2, along with a description of the methodology and the diagnos-  
84 tics. Section 3 evaluates the model realism by comparing observed and simulated fields, including the SST-WS  
85 coupling characteristics and their spatial and seasonal variations. The WS intensity dynamical response to the  
86 SST mesoscale field is analyzed in section 4. We evidenced two concurrent effects affecting the WS : one related  
87 to the Turbulent Kinetic Energy (TKE) modifications, and anotherone due to wind shear anomalies. The origin  
88 of these wind anomalies is studied through a momentum balance analysis. Results are discussed in section 5  
89 before concluding in section 6.

## 90 **2 Methodology**

### 91 2.1 Observational dataset

92 Satellite observations are used to characterize the SST-WS coupling and to evaluate the realism of the model  
93 solution. WS data are from the QSCAT scatterometer (Dunbar et al, 2006). We use the daily product gridded

94 at 50 km for the period 2000-2009 processed by the Centre ERS d'Archivage et de Traitement (CERSAT,  
95 2002). The Microwave Optimally Interpolated (MW OI) SST is a merged product from different satellite data,  
96 processed by Remote Sensing System and available at [www.remss.com](http://www.remss.com). It provides daily data at  $0.25^\circ$  resolution.  
97 We use data for the 2000-2009 period. To evaluate the model solution heat fluxes and cloud cover, we use the  
98 short-wave ocean surface radiation from the International Satellite Cloud Climatology Project (ISCCP, Schiffer  
99 and Rossow, 1983; Zhang et al, 2004) for the year 2007. Its spatial resolution is  $2.5^\circ$ . Data are available through  
100 the OAFlux project (<http://oafux.whoi.edu>). Rawinsonde data from the VOCALS-REx campaign (VAMOS  
101 Ocean-Cloud-Atmosphere-Land Study Regional Experiment; Wood et al, 2011) provide wind velocity and air  
102 temperature observations in the PBL along a  $20^\circ\text{S}$  zonal section for the time period between October 28th,  
103 2008 and November 3rd, 2008.

## 104 2.2 Regional Ocean-Atmosphere Coupled Model

### 105 *2.2.1 Atmospheric model*

106 The atmospheric component is the Weather Research and Forecasting (WRF) model using the ARW (Advanced  
107 Research WRF) solver (Skamarock and Klemp, 2008) in its 3.6 version. WRF is a regional model solving the  
108 fully compressible non-hydrostatic Euler equations on a C-grid with terrain-following mass vertical coordinate.  
109 The atmospheric grid has 60 vertical sigma levels with the top of the atmosphere located at 50 hPa. We increase  
110 the WRF default vertical resolution defining 21 levels in the first  $\sim 1000$  m. The horizontal resolution is  $1/12^\circ$ .  
111 Time step is 20 s. A third order Runge-Kutta time-integration scheme and a 5th-order upwind-biased advection  
112 scheme in space are used.

113 WRF allows for the testing of a large range of parameterizations. Our configuration uses Goddard short-  
114 wave flux scheme (Chou and Suarez, 1994), the longwave Rapid Radiative Transfer Model (RRTM; Mlawer et al,  
115 1997) and the "WSM6" microphysics scheme (Hong and Lim, 2006). Cumulus are parameterized by the Betts-  
116 Miller-Janjic scheme (Janjic, 1994). We use the unified NOAA land surface model with the surface layer scheme  
117 from the fifth-generation Mesoscale Model (MM5, Chen and Dudhia, 2001). To represent the PBL physics, the

118 Mellor-Yamada-Nakanishi-Niino (MYNN) 2.5 level (Nakanishi and Niino, 2009) scheme is selected, associated  
 119 with its corresponding MYNN surface scheme. In our region, this PBL parameterization produces the most  
 120 realistic simulation (see Sec. 3). As Perlin et al (2014) showed that the SST-WS coupling intensity is sensitive  
 121 to the WRF PBL scheme, we also perform a simulation using the Yonsei University (YSU, Hong et al, 2006)  
 122 PBL scheme and the MM5 surface layer parameterization (Paulson, 1970). We choose YSU for two reasons.  
 123 First, we tested several PBL schemes and YSU gives the second most realistic simulation (after MYNN), both  
 124 for regional climate mean state and coupling characteristics (see Sec. 4.3). Second, MYNN and YSU derive  
 125 from two different momentum turbulent mixing theories. In MYNN, momentum mixing is parameterized by a  
 126 Reynolds turbulent stress  $\vec{\tau}$  at the layers interface, proportional to  $\partial_z \vec{v}$ , the vertical shear of horizontal velocity  
 127 (all wind speed and velocities presented in this article referred to the horizontal wind) :

$$\vec{\tau} = \rho K_M \partial_z \vec{v} \quad (2)$$

128 with  $\rho$  the air density,  $K_M$ , the momentum vertical diffusion coefficient. In YSU, other terms are included to  
 129 represent the contribution of large-scale eddies to the total flux (Hong and Pan, 1996) and the entrainment flux  
 130 (Hong et al, 2006). In MYNN,  $K_M$  is locally computed on each grid point using a TKE budget (that includes  
 131 air/sea turbulent fluxes). This differs from YSU where the vertical profile of  $K_M$  is determined at each horizontal  
 132 grid point using the PBL height and the air/sea turbulent fluxes. A more detailed comparison between these  
 133 two momentum turbulent mixing parameterizations can be found in Perlin et al (2014).

134 Initial and open boundary conditions are extracted from ERA-interim reanalysis (Dee et al, 2011) 6 hours  
 135 averages with an horizontal resolution of  $\sim 3/4^\circ$ . We consider a 1-day spinup period for the coupled simulations  
 136 as the focus here is on PBL structures adjusting quickly to the oceanic mesoscale.

### 137 2.2.2 Oceanic model

138 The ocean component is the Nucleus for European Modeling of the Ocean (NEMO, Madec, 2008) model in its  
 139 version 3.4. NEMO is a primitive equations ocean model that has been run in several regional configurations  
 140 (*e.g.* Resplandy et al, 2011; Jouanno and Sheinbaum, 2013; Benshila et al, 2014). The ocean vertical grid has

141 75 z-levels, with 25 levels above 100m. The vertical resolution ranges from 1 m at the surface to 200 m at the  
 142 bottom where a partial step representation of the topography (Adcroft et al, 1997) is used. The time step is 400  
 143 s.

144 Horizontal tracer and momentum advection is treated with an upstream-biased (UBS) third order scheme  
 145 (Farrow and Stevens, 1995; Webb et al, 1998). The vertical tracer flux is evaluated using a total variance  
 146 dissipation scheme (Lévy et al, 2001) and the momentum vertical advection is a simple 2nd order centered  
 147 scheme. As the UBS scheme already includes an intrinsic diffusion, we are not using any explicit horizontal  
 148 diffusion/viscosity in these simulations. The vertical mixing is parameterized using an improved version of  
 149 Turbulent Kinetic Energy, closure scheme (Blanke and Delecluse, 1993; Madec, 2008).

150 Lateral boundary conditions are 5-day averages for temperature, salinity and velocity coming from simu-  
 151 lations performed in the Drakkar project (global oceanic simulation ORCA025-B83 performed with NEMO at  
 152  $0.25^\circ$  horizontal resolution and 46 vertical levels; Dussin et al, 2009). A non-coupled spin-up was performed  
 153 using an oceanic  $1/12^\circ$  regional simulation forced by ERAinterim over the 1990-2006 period. Oceanic states of  
 154 December 31, 2004 (for the simulation starting in 2005) and 2006 (for simulations starting in 2007) are used as  
 155 initial conditions.

### 156 *2.2.3 Ocean-atmosphere coupling and simulations*

157 WRF and NEMO are coupled through the Ocean Atmosphere Sea Ice Sol (OASIS3-MCT, Valcke et al, 2013)  
 158 coupler, as done by Samson et al (2014). Coupling frequency is  $1 \text{ h}^{-1}$ . The same horizontal resolution ( $1/12^\circ$ )  
 159 and the same horizontal grid ( $[10^\circ\text{N} - 30^\circ\text{S}]$  and  $[100^\circ\text{W} - 60^\circ\text{W}]$ ) are used for NEMO and WRF. There  
 160 is no restoring of any kind in the atmosphere or in the ocean. Fig. 1 presents a scheme of the vertical levels  
 161 distribution in the coupled model. Ocean velocity in the surface layer is named  $\vec{v}_1^o$ . In the atmosphere,  $z_N$  is  
 162 the height of level N, where wind velocities  $\vec{v}_N^a$  and the air density  $\rho(z_N)$  are defined. The height of the first  
 163 atmospheric level is  $z_1 = 10 \text{ m}$ . The turbulent stress  $\vec{\tau}_N^a$  is defined at the top of layer N.

164 The air/sea stress conditions (*i.e.* WS) are computed in surface layer parameterization of WRF. Both MYNN  
 165 and MM5 schemes are based on the Monin-Obukov similarity theory (Monin and Obukhov, 1954). WS is

166 expressed by :

$$\vec{\tau}_s = \rho(z_1) u^{*2} \frac{\vec{v}_1}{\|\vec{v}_1\|} \quad (3)$$

$$u^* = \frac{k_0 \|\vec{v}_1\|}{\ln\left(\frac{z_1}{z_0}\right) - \psi\left(\frac{z_1}{L}\right)} \quad (4)$$

167 with  $k_0$  the Von Karman constant,  $z_0$  the roughness length.  $\psi$ , the stability function, depends on the chosen  
 168 scheme and  $L$ , the Monin-Obukov length. However, at the air-sea interface, the WS actually depends on the  
 169 surface wind velocity relative to the surface ocean current (Dawe and Thompson, 2006; Song et al, 2006). This  
 170 impacts the WS mesoscale structure (Chelton et al, 2004). In order to take this effect into account, the stress  
 171 conditions at air-sea interface are modified : equations (3) and (4) are computed using  $\vec{v}_1 - \vec{v}_1^o$  instead of  $\vec{v}_1$   
 172 (Lemarié, 2015). This requires modifications in several WRF routines that are now available in the latest model  
 173 releases (from version 3.6).

174 Two simulations using different PBL schemes are performed: a 4-year simulation (for the period 2005-2008)  
 175 using the MYNN PBL scheme named CPLM and a 1-year simulation (for the year 2007) with the YSU PBL  
 176 scheme named CPLY (see Sec. 3.3.1).

## 177 2.3 SST and WS fields processing

### 178 2.3.1 Fields regridding

179 Observed and simulated WS and SST fields have different spatial resolutions. For an accurate comparison,  
 180 the fields are regridded on the same  $0.5^\circ$  grid (for each QSCAT data point, the model field is averaged over  
 181 the surrounding  $0.5^\circ$  square box). We refer to these fields as CPLM50 and CPLY50. To study the coupling  
 182 characteristics in the observations, the  $0.25^\circ$  MW OI SST is also regridded on the  $0.5^\circ$  QSCAT grid. Finally,  
 183 to directly compare the simulated and MW OI SST, we also regrid the model field on the  $0.25^\circ$  MW OI grid.  
 184 We refer to these fields as CPLM25 and CPLY25 SST.

### 2.3.2 Preprocessing for SST-WS coupling analysis

In the coastal region, orographic effects create WS mesoscale anomalies more intense than the SST-induced ones (Boe et al, 2011; Renault et al, 2015). Desbiolles et al (2014) showed that in EBUS a nearshore strip of at least 100 km should be removed to properly study the SST influence on WS mesoscale anomalies. Here, we discard the first 150 km nearshore from the coupling characteristics analysis.

To isolate the mesoscale structures, SST and WS intensity daily fields are smoothed using a Gaussian spatial filter with a standard deviation of 150 km. Mesoscale anomalies of a field  $\phi$  (SST or  $\|\vec{\tau}_s\|$ ) are defined as  $\phi' = \phi - \bar{\phi}$ , with  $\bar{\phi}$  the smoothed field. In the following, we simply refer to  $\phi'$  as anomalies and large-scale field refers to the smoothed field  $\bar{\phi}$ . Figure 2 represents CPLM SST and WS intensity anomalies for July 2007. The filtering efficiently removes the large scale patterns and reveals correlated structures between the two fields, consistently with relation (1).

### 2.3.3 SST-WS coupling characteristics

Relation (1) between SST and WS intensity anomalies is evaluated and characterized during (late) austral summer and winter. Following Chelton et al (2007), we use 29-day averaged periods (to remove weather synoptic variability) overlapping with 7-day intervals. For summer (winter) 13 periods from January to April (July-October, respectively) are selected. The WS intensity is computed using WS daily mean intensity averaged over 29-day periods

A scatterplot of WS intensity anomalies as a function of SST anomalies is generated using all points of the 13 maps. The scatterplot correlation  $R$  indicates the strength of the linear relationship. Correlations are significant within a 95 % confidence level. They are presented in section 3.3.1 (see Table 1).

As in previous studies (*e.g.* Chelton et al, 2001; Desbiolles et al, 2014; Perlin et al, 2014), the SST axis is divided into 0.1 °C intervals and the WS intensity anomaly means and standard deviations are computed for each SST interval. A “binned” scatterplot is generated using these means and standard deviations. Intervals containing less than 1 % of the points are discarded. An example can be found on Figure 7 in Section 3.3.1.

209 We compute the binned scatterplot slope, *i.e.* the Regression Coefficient (RC) associated to relation (1). RC  
210 represents the intensity of the WS response to a given SST anomaly. In the following we describe the coupling  
211 characteristics R and RC in the PCS.

## 212 2.4 Composite of vertical profiles

213 To study the PBL response to the SST anomalies we compute composites of vertical profiles of air temperature  
214 and wind speed anomalies above warm ( $SST' > 0.1 \text{ }^\circ\text{C}$ ) and cold ( $SST' < -0.1 \text{ }^\circ\text{C}$ ) SST anomalies (Sec. 4.1.2  
215 and 5.2). Wind speed increases with height, reaching its maximum  $Z_{max}$  at a few 100-m height.  $Z_{max}$  varies  
216 spatially over the domain. To obtain composite profiles, the vertical axis is rescaled for each profile so that  
217  $Z_{max} = Z_{max}^{mean}$ , with  $Z_{max}^{mean}$  the height of the maximum of the wind speed mean profile (spatial mean over the  
218 domain). The same methodology is applied to air temperature using the inversion height (Sec. 5.2).

## 219 3 Model realism and mesoscale coupling description

### 220 3.1 Mean state

221 The realism of our reference simulation (CPLM) is first evaluated by comparing annual means of the WS and  
222 SST fields (Fig. 3). A realistic mean state is important to study the mesoscale coupling as it affects the intensity  
223 of the WS response to SST anomalies (see O'Neill et al, 2012, and Sec. 3.3.2 and 4.2). Figure 3 shows that  
224 the regional patterns are reproduced by the model. South of the equator, the wind blows north-westward with  
225 a stronger intensity near the Chile coast at  $30 \text{ }^\circ\text{S}$  and between  $6 \text{ }^\circ\text{S}$  and  $24 \text{ }^\circ\text{S}$  offshore. Near the coast, the  
226 wind is alongshore and its intensity decreases shoreward. This decrease appears to be slightly overestimated  
227 by the model in some regions (*e.g.* the  $[7^\circ \text{ S} - 13 \text{ }^\circ\text{S}]$  coastal segment) when compared to QSCAT data. The  
228 SST field presents a cold tongue along the Peru-Chile coast, characteristic of a wind-driven coastal upwelling.  
229 Simulated SST are colder ( $\sim 1 \text{ }^\circ\text{C}$ ) than the satellite observations close to the coast. Note that the 25 km MW  
230 IO SST misses part of the upwelling structure in the very nearshore. So, within a coastal strip, the SST has  
231 been extrapolated from offshore and the actual SST is expected to be colder in the central Peru coastal region.

232 South of the equator, spatial correlations between observed and simulated fields are 0.97 for WS intensity and  
233 0.95 for SST. Along the equator, CPLM underestimates the cold tongue extension and presents a 2 °C warm  
234 bias, associated to an overestimated WS intensity (0.008 N m<sup>-2</sup> bias). In the northern part of the domain the  
235 model solution is less realistic: WS intensity is  $\sim 0.02$  N m<sup>-2</sup> too weak and the SST is up to 2 °C too warm.  
236 This is because the atmospheric model parameterizations, chosen to realistically reproduce the PCS climate,  
237 are certainly less adequate for the trade winds convergence zone and intense deep convection areas.

238 Common biases when modeling the lower atmosphere in EBUS are an unrealistic downward short-wave flux  
239 above the ocean (Ma et al, 1996; Davey et al, 2002; Meehl et al, 2005) and an underestimation of the low  
240 cloud cover (*e.g.* Wyant et al, 2010; De Szoeki et al, 2012). In coupled models, this can lead to a large SST  
241 bias (De Szoeki et al, 2010). CPLM flux is compared to ISCCP data in Fig. 4. It shows a large pattern of low  
242 short-wave ( $\sim 175$  W m<sup>-2</sup>) off the Peru-Chile coast from 12 °S to 30 °S that can be due to the presence of low  
243 clouds. West of 90 °W, the short-wave flux is higher. North of the equator, the observed low short-wave strip  
244 along 6 °N and the minimum in the Panama Bight region are poorly simulated. This may explain the warm  
245 SST bias in this area (Fig. 3).

246 The large-scale wind vertical structure has a big impact on the atmospheric response to SST mesoscale  
247 patterns (see Sec. 4.1). Zonal sections at 20 °S of the wind velocities are shown on Fig. 5. The simulated wind  
248 presents similar structures than the VOCALS-REx observations. Near the surface, the meridional wind flows  
249 northward with a maximum jet at  $\sim 900$  hPa and its intensity decreases nearshore (Fig. 5a and b). This decrease  
250 is somewhat underestimated by the model, contrarily to what is seen on Fig. 3. This difference may be attributed  
251 to the fact that the comparisons in Figs. 3 and 5 use different datasets (QSCAT and in situ rawinsonde data)  
252 over different periods (annual mean and several days average). At height, a southward meridional velocity is  
253 associated to the poleward branch of the Hadley cell. The height of the wind reversal is  $\sim 500$  hPa at 85 °W  
254 both in model and observations and it decreases toward the shore (at 72 °W) reaching  $\sim 980$  hPa in observations  
255 and  $\sim 940$  hPa in the model. Near the surface, the zonal wind (Fig. 5c and d) flows westward and decreases  
256 nearshore. At height, it flows eastward and the reversal height decreases from 700 hPa at 85 °W to  $\sim 950$  hPa  
257 at 72 °W. These patterns are captured in the model solution.

## 3.2 Mesoscale activity

Statistics of the mesoscale fields are examined for simulated and observed WS intensity and SST. Anomalies, as defined in Sec. 2.3.2, are computed for each monthly field of CPLM25 SST, CPLM50 WS intensity and observations for the year 2007.

Both the probability density function (PDF) and the monthly-mean absolute values show that SST anomalies have more extreme values in the model solution than in observations (Fig. 6a, b). CPLM25 captures well the seasonal cycle of the mean SST anomaly with enhanced (reduced) anomalies in autumn (summer, respectively). Similar results are obtained for WS intensity anomalies (Fig. 6c, d): CPLM50 wind anomalies are more intense than in observations but have the same seasonal variability. Note that having stronger WS intensity and SST anomalies is consistent with relation (1), assuming realistic coupling characteristics (Sec. 3.3). Interestingly, WS intensity and SST anomalies seasonal cycles are not in phase (maximum in winter for WS intensity and in fall for SST). This indicates that coupling characteristics  $R$  and  $RC$  vary in time (Sec. 3.3).

## 3.3 SST-WS mesoscale coupling

### 3.3.1 Comparison between model and observations

WS intensity and SST fields from CPLM, CPLM50 and observations are processed as described in Sec. 2.3 to examine the mesoscale coupling characteristics. Binned scatterplots for austral winter in the Peru region (from 9 °S to 18 °S and from 95 °W to 150 km offshore; red box in Fig. 2) are shown on Fig. 7. All panels exhibit a clear linear relationship between SST and WS intensity anomalies.  $R$  and  $RC$  between WS intensity and SST are larger ( $\sim 50\%$  for  $RC$ ) in the model ( $R=0.77$ ) than in the observations ( $R = 0.59$ ). The model overestimates both the intensity of the SST anomalies (Sec. 3.2) and  $RC$ . This may be why the part of the total WS intensity variance explained by relation (1), *i.e.*  $R^2$ , is larger in the model than in the observations. Note that the regridding does not affect much the WS intensity dependence to the SST, as  $R$  and  $RC$  are not very different for CPLM and CPLM50.

281 The same diagnostics are computed for the summer season and for the southern part of our domain (“Chile”  
 282 region, from 18 °S to 27°S and from 150 km offshore to 95 °W; Fig. 2). Results are presented in Table 1. CPLM  
 283 and CPLM50 values are always close. Again, R is smaller in observations than in the model, except off Chile  
 284 in summer. RC values are higher in the model than in the observations in winter ( $\sim 50\%$  and  $25\%$  larger for  
 285 Peru and Chile, respectively) while they are very close in summer<sup>1</sup>. The simulation and the observations share  
 286 similar spatial and temporal variability. First, the coupling characteristics are weaker in summer than in winter.  
 287 This seasonal cycle is also observed for the entire QSCAT period (2000-2009) and in the 4 years (2005-2008) of  
 288 CPLM (not shown). Second, R and RC are larger off Peru than off Chile.

289 As evidenced by Chelton et al (2001), spatial derivatives of (1) lead to :

$$\text{div}(\vec{\tau}_s') \propto \text{grad}_{dw}(SST') \quad (5)$$

290

$$\text{curl}(\vec{\tau}_s') \propto \text{grad}_{cw}(SST') \quad (6)$$

291 with  $\text{curl}(\vec{\tau}_s') = \vec{\nabla} \wedge \vec{\tau}_s' \cdot \vec{k}$ , the vertical component of the stress curl,  $\vec{k}$  being the vertical unit vector.  
 292  $\text{grad}_{dw}(SST')$  and  $\text{grad}_{cw}(SST')$  are the downwind and crosswind projections of the gradient, respectively :  
 293  $\text{grad}_{dw}(SST') = \|\vec{\text{grad}}(SST')\| \cos(\theta)$  and  $\text{grad}_{cw}(SST') = \|\vec{\text{grad}}(SST')\| \sin(\theta)$ ,  $\theta$  being the counterclockwise  
 294 angle from  $\vec{\text{grad}}(SST')$  to  $\vec{\tau}_s'$ . We have examined these relations and results are summarized in Tables 2 and  
 295 3. As for relation (1), R values are overestimated in the model. Observed and simulated RC are very close in  
 296 summer while in winter the simulated RC is  $\sim 30\%$  too large. The spatial and seasonal variability are similar  
 297 in the model and in observations: R and RC are stronger in winter than in summer and slightly higher off Peru  
 298 than off Chile, except for relation (6) in summer.

299 In contrast with our results, Putrasahan et al (2013) obtained stronger coupling characteristics in summer  
 300 than in winter. However, they used a different methodology in the computation of the binned scatterplot. They  
 301 included bins with extreme SST gradients that contains very few points. This might give an important weight to  
 302 extreme SST values and might influence RC values. Moreover, they computed the correlations from the binned

<sup>1</sup> Perlin et al (2014) tested several PBL schemes using the 3.3 version of WRF. They obtained a large overestimation of RC with MYNN, inconsistent with our results. Improvements in this parameterization between version 3.3 and 3.6 reduces RC (not shown).

303 scatterplots while we did it directly on the SST and WS intensity fields before binning (correlations of our  
 304 binned scatterplot are always higher than 0.98).

### 305 *3.3.2 Spatial variations of the coupling characteristics*

306 To further investigate the spatial variations of the coupling characteristics, we take advantage of the high  
 307 resolution of CPLM to map R and RC for relation (1). Every 12 points of the horizontal grid, we estimate the  
 308 coupling diagnostics using all points included in a 450 km-large square (moving) box centered on this grid point.

309 Only RC values for winter are shown in Fig. 8 (the R map presents similar patterns). The RC map presents  
 310 a large area off Peru with values  $\sim 1.5 \cdot 10^{-2} \text{ N m}^{-2} \text{ } ^\circ\text{C}^{-1}$ . Off Chile, RC values are  $\sim 1.3 \cdot 10^{-2} \text{ N m}^{-2} \text{ } ^\circ\text{C}^{-1}$   
 311 nearshore while they are much smaller ( $< 0.8 \cdot 10^{-2} \text{ N m}^{-2} \text{ } ^\circ\text{C}^{-1}$ ) offshore. Near the coast, the northern and  
 312 southern regions are separated by a minimum ( $\sim 0.4 \cdot 10^{-2} \text{ N m}^{-2} \text{ } ^\circ\text{C}^{-1}$ ) around  $20^\circ\text{S}$ .

313 Several factors are possibly affecting the coupling characteristics. Chelton et al (2007) and Castelao (2012)  
 314 showed evidence that the air-sea mesoscale coupling is more efficient under steady wind conditions. The surface  
 315 wind steadiness (St) is defined as

$$St = \frac{\|\langle \vec{v}_1 \rangle\|}{\langle \|\vec{v}_1\| \rangle} \quad (7)$$

316 with  $\langle \rangle$  the temporal averaging. St is close to 1 when the wind is steady, and decreases when the wind often  
 317 changes direction. Winter St is represented on Figure 8. Off Chile, low RC values correspond to the region with  
 318 lower ( $< 0.9$ ) steadiness. However, the steadiness spatial distribution does not explain the low RC north of  $9^\circ\text{S}$   
 319 and nearshore around  $20^\circ\text{S}$ . O'Neill et al (2012) showed that RC also depends on the large-scale wind intensity.  
 320 The large RC values off Peru corresponds to the strongest wind area ( $> 8 \text{ m s}^{-1}$ ) while the nearshore Chile  
 321 region south of  $20^\circ\text{S}$  has a  $7.5 \text{ m s}^{-1}$  wind intensity and intermediate RC values. Finally, the nearshore region  
 322 near  $20^\circ\text{S}$  and the smallest RC region off Chile correspond to the weakest wind ( $< 7 \text{ m s}^{-1}$ ).

## 4 Mechanisms behind the coupling and its seasonal cycle

To investigate the coupling mechanisms, we now focus on the Peru region, which presents relatively homogeneous coupling characteristics. We first study the PBL response to the SST anomalies during winter (July 2007) as the coupling intensity is stronger during this season.

### 4.1 Mechanisms driving the SST feedback on the WS

WS intensity anomalies are approximated by turbulent stress intensity anomalies  $\tau'_1$  at the top of the first atmospheric model layer (*i.e.* 20 m in our configuration)<sup>2</sup> both fields are highly correlated ( $>0.99$ ) and are related by  $\tau'_s = \alpha\tau'_1$  with  $\alpha = 0.95$ . The turbulent stress  $\vec{\tau}'_1$  is proportional to  $K_M$  and the wind velocity vertical shear (equation (2)). Figure 9 presents vertical profiles of the mixing coefficient  $K_M$  and wind speed.  $K_M$  increases with height, reaching its maximum at 300 m. It decreases above and vanishes around 1000 m. Warm (cold) anomalies are associated with enhanced (reduced, respectively) turbulent mixing. Large-scale wind speed profiles presents a positive vertical shear (Fig. 9b). This is a necessary condition to the momentum transfer from upper layers to lower layers by the so-called downward mixing mechanism (*e.g.* Hayes et al, 1989; Wallace et al, 1989). The composite of the wind speed anomalies above warm SST anomalies (Fig. 9c) exhibits an enhanced wind speed in the lower part of the PBL while the wind speed is reduced in the upper part of the PBL. These wind speed anomalies led to a decreased wind speed vertical shear. The symmetrical situation occurs above cold SST anomalies. Features evidenced in Fig. 9 are consistent with the observations from Hashizume et al (2002) in the EEP.

#### 4.1.1 Decomposition of the WS anomalies

Larger (smaller)  $K_M$  over warm (cold, respectively) waters tends to increase (decrease) the turbulent stress  $\vec{\tau}$  according to equation (2). Conversely, a weaker (stronger) wind shear tends to decrease (increase) it. Thus,

<sup>2</sup> The WS  $\vec{\tau}'_s$  being the turbulent stress  $\vec{\tau}$  condition at the air-sea interface, the intensity of

these two effects can compensate each other. To investigate this,  $\vec{\tau}$  is decomposed as follows :

$$\vec{\tau} = \rho K_M \partial_z \vec{v} = \underbrace{\rho K_M \overline{\partial_z \vec{v}}}_{\vec{\tau}_a} + \underbrace{\rho K_M \partial_z \vec{v}'}_{\vec{\tau}_b} \quad (8)$$

$\vec{\tau}$  denotes the large-scale field (a Gaussian filter is applied as described in section 2.3.2) and  $'$  denotes the mesoscale anomalies. A similar decomposition for the turbulent stress shear was introduced by Koseki and Watanabe (2010). Our decomposition separates the stress proportional to the wind shear anomalies  $\vec{\tau}_b$  from  $\vec{\tau}_a$  (which does not depend on  $\partial_z \vec{v}'$ ). In the following, we focus on the stress anomalies, so equation (8) was filtered (see section 2.3.2) to isolate mesoscale fields :  $\vec{\tau} = \vec{\tau}_a + \vec{\tau}_b$ . Note that :  $\vec{\tau}_a = (\rho K_M \overline{\partial_z \vec{v}})' = (\rho \overline{K_M} \overline{\partial_z \vec{v}} + \rho K_M' \overline{\partial_z \vec{v}})' = \rho K_M' \overline{\partial_z \vec{v}}$ . The mesoscale anomalies  $\vec{\tau}_a$  are entirely created by the mixing coefficient anomalies.

In the MYNN formulation, the mixing coefficient is parameterized using a TKE formulation. The positive (negative) anomalies of  $K_M$  above warm (cold) SST anomalies shown in Fig. 9a are due to positive (negative) TKE anomalies (not shown). A TKE budget examination indicates that TKE anomalies are caused at the first order by the temperature turbulent flux (the buoyancy production term) anomalies with a negligible contribution of the wind shear term (not shown). This confirms that equation (8) adequately separates the turbulent stress independant from the wind shear ( $\vec{\tau}_a$ ) from the stress proportional to the wind shear anomalies ( $\vec{\tau}_b$ ). SST anomalies create air temperature anomalies and drive TKE anomalies ( $K_M'$ ) through atmospheric stability modifications. It leads to turbulent stress anomalies  $\vec{\tau}_a$ . This modifies the momentum balance (Sec. 4.1.2) and generates wind shear anomalies that in return affect the turbulent stress  $\vec{\tau}_b$  (but not TKE or  $K_M$ ).

As the turbulent stress anomalies are mainly downwind (not shown), (8) gives  $\tau'_1 \approx \tau'_a + \tau'_b$ , with  $\tau'_1$ ,  $\tau'_a$  and  $\tau'_b$  the norms of  $\vec{\tau}'_1$ ,  $\vec{\tau}'_a$  and  $\vec{\tau}'_b$ , respectively. Note that this also means that  $\|\partial_z \vec{v}'\| \approx (\partial_z \vec{v}') \cdot \frac{\vec{v}'}{V} \approx \partial_z V$ . Figure 10 presents the three terms (at 20 m height).  $\tau'_1$  and SST anomalies are highly correlated (R=0.71), with a RC of  $0.7 \cdot 10^{-2} \text{ N m}^{-2} \text{ }^\circ\text{C}^{-1}$ . The SST anomalies create  $K_M$  anomalies that induce a positively correlated  $\tau'_a$  pattern (with RC  $\approx 2.0 \cdot 10^{-2} \text{ N m}^{-2} \text{ }^\circ\text{C}^{-1}$ ). Wind shear anomalies generated by such mixing induce instead a  $\tau'_b$  pattern with opposite sign that partly compensates  $\tau'_a$  (with RC  $\approx -1.3 \cdot 10^{-2} \text{ N m}^{-2} \text{ }^\circ\text{C}^{-1}$ ).

363 *4.1.2 What drives wind speed vertical shear anomalies ?*

364 We now investigate the mechanisms generating near-surface wind shear anomalies. In particular, we examine  
 365 whether the wind speed is modified because of pressure or turbulent stress perturbations. To this aim, we first  
 366 investigate why the near-surface wind speed is faster (slower) above warm (cold, respectively) water and why  
 367 wind anomalies change with height (see Fig. 9c).

368 The wind velocity variations are driven by the momentum balance :

$$\partial_t \vec{v} + (\vec{v} \cdot \vec{\nabla}) \vec{v} = \partial_z \left( \frac{\vec{\tau}}{\rho} \right) - f \vec{k} \wedge \vec{v} - \frac{1}{\rho} \vec{\text{grad}} P \quad (9)$$

369 with  $f$  the Coriolis parameter and  $P$  the pressure. The term  $\partial_t \vec{v} + \vec{v} \cdot \vec{\nabla} \vec{v}$  represents the Lagrangian acceleration  
 370 of an air parcel.  $\partial_z \left( \frac{\vec{\tau}}{\rho} \right)$  represents the tendency due to the turbulent vertical mixing of momentum.  $-f \vec{k} \wedge \vec{v}$  is  
 371 the Coriolis force and  $-\frac{1}{\rho} \vec{\text{grad}} P$  the pressure gradient. Following O'Neill et al (2010), (9) can be written using  
 372 natural coordinates. Here we only focus on the downwind momentum budget:

$$V \text{grad}_{dw}(V) = \frac{\vec{v}}{V} \cdot \partial_z \left( \frac{\vec{\tau}}{\rho} \right) - \frac{1}{\rho} \text{grad}_{dw}(P) \quad (10)$$

373 with  $V = \|\vec{v}\|$  and considering that  $\frac{\vec{v}}{V} \cdot (\partial_t \vec{v}) \ll V \text{grad}_{dw}(V)$ . (10) describes the driving of the Lagrangian  
 374 acceleration following a streamline  $\partial_t V + V \text{grad}_{dw}(V)$ , that can be approximated by  $V \text{grad}_{dw}(V)$  as  $\partial_t V \ll$   
 375  $V \text{grad}_{dw}(V)$  (not shown).

376 Time averaging of equation (10) terms for July 2007 (see Appendix) are computed and spatially filtered to  
 377 analyze mesoscale anomalies. Near the surface, downwind wind speed gradient are colocated with downwind  
 378 SST gradients (not shown) : air parcels are decelerated (accelerated) when flowing from warm to cold (cold  
 379 to warm, respectively) waters, which is consistent with the surface wind anomalies shown in Fig. 9c. Hence,  
 380 the acceleration vertical shear  $\partial_z(V \text{grad}_{dw}(V))$  above the frontal regions is responsible for the wind speed  
 381 shear anomalies above SST anomalies. In the following we analyze the mechanisms responsible for wind speed

382 mesoscale anomalies using (10) and its vertically derived expression :

$$\partial_z(V\text{grad}_{dw}(V)) = \partial_z\left(\frac{\vec{v}}{V} \cdot \partial_z\left(\frac{\vec{\tau}}{\rho}\right)\right) - \partial_z\left(\frac{1}{\rho}\text{grad}_{dw}(P)\right) \quad (11)$$

383 We compute composites of the different terms above the regions of positive ( $\text{grad}_{dw}SST' > 2 \cdot 10^{-5} \text{ }^\circ\text{C}$   
 384  $\text{m}^{-1}$  for cold to warm transition) and negative ( $\text{grad}_{dw}SST' < -2 \cdot 10^{-5} \text{ }^\circ\text{C m}^{-1}$  for warm to cold transition)  
 385 downwind SST gradient anomalies. Vertical profiles of the anomalies of the terms in (10) are represented on Fig.  
 386 11. Momentum is redistributed in the PBL as the air parcels flowing from warm to cold waters are decelerated  
 387 below 100 m and accelerated above (Fig. 11a). The deceleration is strongest near the surface (Fig. 11a), creating  
 388 a strong near-surface wind shear. Below 100 m, the vertical mixing term largely dominates over pressure (Fig.  
 389 11a). Thus, the deceleration and its vertical shear (Fig. 11b) in the lower layers are mainly due to the effect  
 390 of turbulent stress shear perturbations, while acceleration of the wind above 100 m is driven by the pressure  
 391 gradient. The pressure gradient role is further discussed in section 5.2.

392 The cold to warm composites (Fig. 11c) present a symmetrical situation : lower layers (below 200 m) are  
 393 accelerated while upper layers are decelerated. Near the surface, the pressure gradient is stronger than in the  
 394 warm to cold case. However, the turbulent stress shear remains the main forcing of the acceleration, while above  
 395 50 m, the pressure effect becomes important (Fig. 11c).

396 In conclusion, in both cases, below  $\sim 100$  m, the wind shear anomalies are driven by the turbulent stress  
 397 perturbations, while the effect of the pressure gradient is an order of magnitude weaker. Previous studies have  
 398 also examined the momentum budget over SST fronts. Consistency between our results and theirs are further  
 399 discussed in Sec. 5.2.

## 400 4.2 Seasonal variations of the SST feedback on WS

### 401 4.2.1 Origin of the seasonal variations

402 We now use the stress decomposition (Sec. 4.1.1) to explain the seasonal variation of the coupling strength  
 403 (Table 1). Table 4 presents the RC between SST anomalies and  $\tau'_1$ ,  $\tau'_a$  and  $\tau'_b$  during winter (July) and summer

404 (January). Both  $\tau'_a$  and  $\tau'_b$  responses are increased by  $\sim 60\%$  from summer to winter and so is the total coupling  
 405 strength (RC between SST' and  $\tau'_1$ ). Figure 12 helps to understand whether  $\tau'_a$  and  $\tau'_b$  seasonal variation can be  
 406 attributed to mixing coefficient and/or wind shear variations.

407 The binned scatterplot of  $K'_M$  with respect to SST' (Fig. 12a) shows that RC changes little between winter  
 408 and summer ( $1.24$  and  $1.45 \cdot 10^{-2} \text{ m}^{-2} \text{ s}^{-1} \text{ }^\circ\text{C}^{-1}$ , respectively, *i.e.* a  $14 \%$  increase). Thus, the stronger  $\tau'_a$   
 409 response in winter is related to the large-scale wind shear seasonal variation (the intensity of  $\overline{\partial_z \vec{v}}$  at  $20 \text{ m}$  is  $\sim$   
 410  $1.1 \cdot 10^{-2} \text{ s}^{-1}$  in winter and  $\sim 0.7 \cdot 10^{-2}$  in summer, *i.e.* a  $60 \%$  decrease).

411 The binned scatterplot of  $\|\partial_z \vec{v}'\|$  (Fig. 12b) shows that SST anomalies create wind velocity shear anomalies  
 412  $\sim 60\%$  stronger in winter than in summer while the mixing coefficient spatial average changes little ( $5.9$  and  $5.7$   
 413  $10^{-2} \text{ m}^{-2} \text{ s}^{-1}$  in winter and summer, respectively). Thus, the larger  $\tau'_b$  response in winter is mainly driven by  
 414 enhanced wind velocity shear anomalies.

415 Both  $\tau'_a$  and  $\tau'_2$  seasonal changes are attributed to changes in the intensity of the wind velocity shear (large-  
 416 scale and anomalies, respectively) with similar relative amplitudes. Note that the stronger large-scale wind  
 417 velocity shear leads to stronger wind velocity shear anomalies, as given by the momentum balance through  
 418 stronger stress shear anomalies and wind acceleration (not shown). Overall, this implies that the large-scale  
 419 wind shear seasonal variation is responsible for the seasonal variation of the WS response to SST anomalies.

#### 420 4.2.2 Large-scale wind shear

421 We here investigate the origin of the large-scale wind velocity shear seasonal variation. The WS is the boundary  
 422 condition of the turbulent stress at the air/sea interface and its intensity is proportional to the square of the  
 423 surface wind speed ( $V_s^2$ ). Thus, using (2) we obtain

$$V_s^2 \propto \tau_s \sim \|\rho K_M \partial_z \vec{v}'\| \quad (12)$$

424 The horizontal smoothing of (12) leads to  $\overline{V_s^2} \propto \|\overline{\rho K'_M \partial_z \vec{v}'} + \rho \overline{K_M} \overline{\partial_z \vec{v}}\|$ , with  $\overline{K'_M \partial_z \vec{v}'} \ll \overline{K_M} \overline{\partial_z \vec{v}}$ . As  $\overline{K_M}$   
 425 presents weak seasonal variation (see Sec. 4.2.1) we can approximate  $\overline{V_s^2} \propto \|\overline{\partial_z \vec{v}}\|$ .

426 The validity of this relation is shown on Fig. 13a. Monthly means of  $\overline{V_s^2}$  and the wind velocity shear intensity  
427  $\|\overline{\partial_z \vec{v}}\|$  (computed at 20 m, between the first two model levels) are strongly correlated (R=0.97). Thus, the  
428 enhanced large scale velocity vertical shear in winter is associated to the surface wind speed strengthening.  
429 The surface wind winter intensification is a well-known characteristic of the PCS (Fig. 13b) caused by the  
430 equatorward seasonal migration of the South Pacific anticyclone (*e.g.* Strub et al, 1998). These large-scale wind  
431 conditions lead to more efficient momentum vertical mixing during winter in the PCS.

#### 432 4.3 Sensitivity to the PBL parameterization

433 To test the sensitivity of the results to the PBL parameterization, a second simulation (CPLY) was performed  
434 using the YSU PBL scheme (see Sec. 2.2.1). The realism of the large-scale fields is somewhat altered in CPLY  
435 compared to CPLM (not shown). In particular, an overestimated short-wave surface flux results in a warm mean  
436 bias over the Peru-Chile region ( $> 0.5$  °C; not shown) that was not present in CPLM. The mean WS remains  
437 quite realistic in CPLY. Table 1 presents the seasonal coupling characteristics in CPLY. As in CPLM, R and RC  
438 are slightly overestimated with respect to observed values, while regional and seasonal variations are realistic.

439 Figure 9 presents mixing coefficient and wind speed anomalies for CPLM and CPLY.  $K_M$  values are weaker  
440 in CPLY than in CPLM (Fig. 9a) as also shown by Perlin et al (2014) and the large-scale wind speed shear  
441 is stronger in CPLY (Fig. 9b). Warm (cold) anomalies are associated with enhanced (reduced, respectively)  
442 mixing coefficient (Fig. 9a) and positive (negative) surface wind speed anomalies with similar intensities in both  
443 simulations (Fig. 9c). However, in the first 100 m, the wind speed vertical shear anomalies are much weaker in  
444 CPLY. The downwind momentum balance in CPLY shows that the surface acceleration is mainly due to the  
445 turbulent mixing with a negligible contribution of the pressure gradient (not shown). It also shows a weaker  
446 turbulent mixing vertical shear in CPLY than in CPLM which explains the weaker wind speed vertical shear  
447 anomalies.

448 In CPLY, the turbulent stress formulation includes additional terms to equation (2) (see section 2.2.1).  
449 However the anomalies of those terms are negligible (not shown), so the same turbulent stress decomposition as  
450 in CPLM (Sec. 4.1.1) can be applied. Values are given in Table 4 for the winter season. RC for  $\tau_1'$  is reduced in

451 CPLY. Nevertheless, the weaker wind shear anomalies in CPLY create a much weaker compensation by  $\tau'_2$  than  
 452 in CPLM. Overall, the total stress anomalies have a comparable magnitude in the two simulations.

453 Furthermore, as in CPLM, the response of  $K_M$  to SST anomalies is unchanged in CPLY between summer and  
 454 winter (RC  $\sim 0.33$  and  $0.36 \text{ m}^2 \text{ s}^{-1} \text{ }^\circ\text{C}^{-1}$ , respectively). The enhanced large-scale wind shear between summer  
 455 and winter ( $\|\overline{\partial_z \vec{v}}\|$  at 20 m is  $1.4$  and  $2.8 \cdot 10^{-2} \text{ s}^{-1}$ , respectively) explains the seasonal variation of the coupling  
 456 strength in CPLY. This confirms that the role of the large-scale wind shear in modulating the seasonal WS-SST  
 457 response is rather robust and does not depend on the choice of the model parameterizations.

## 458 5 Discussion

### 459 5.1 Sensitivity to the PBL parameterization

460 We have examined the atmospheric response to the SST anomalies with two different PBL schemes. Both  
 461 simulations are rather consistent as they reproduce the observed SST-WS coupling and its seasonal variability  
 462 related to those of the background wind shear. CPLM and CPLY have SST-induced surface wind speed anomalies  
 463 of similar amplitude, created by turbulent mixing anomalies above frontal regions.

464 The major difference between CPLY and CPLM is the wind shear response to the SST anomalies. This  
 465 confirms results from Perlin et al (2014) showing that YSU creates weak wind speed shear anomalies compared  
 466 to the TKE-based parameterizations. Hashizume et al (2002) observed in the EEP an enhanced (reduced) wind  
 467 velocity shear above cold (warm, respectively) SST anomalies, consistent with CPLM results but not with CPLY.  
 468 TKE-based parameterizations like MYNN are more accurate under stable conditions (Hu et al, 2010; Shin and  
 469 Hong, 2011) like those in the PCS. Furthermore, in MYNN,  $K_M$  is computed at each level using local variables  
 470 and, thus, can represent a progressive vertical adjustment to SST anomalies, while YSU prescribes a specific  
 471 (analytical) shape for  $K_M$  vertical profile from the surface forcing (Hong and Pan, 1996) considering that the  
 472 PBL instantaneously adjusts to surface anomalies. As noticed by Perlin et al (2014), this could be a limitation  
 473 to represent accurate mesoscale air-sea interactions. In particular, above a SST front, the horizontal advection

474 does not allow the entire vertical column to adjust to the underlying SST (Small et al, 2008), as assumed in  
475 YSU. This may explain the weak vertical wind velocity shear anomalies found in CPLY.

## 476 5.2 Role of the pressure gradient

477 In our study, near surface pressure gradient anomalies are weak above fronts (Fig. 11), as described in several  
478 observational campaigns (Small et al, 2008). The momentum balance analysis shows that, near the surface, the  
479 wind acceleration is mainly due to momentum turbulent mixing and not to pressure gradients. This is consistent  
480 with results from idealized studies of Spall (2007b), in the case of strong wind at low latitudes, and Kilpatrick  
481 et al (2014) with a comparable experimental framework. Using Large Eddy Simulations, Skillingstad et al (2006)  
482 also showed that the turbulent mixing was the dominant term explaining the wind speed variations. These results  
483 contrast with Small et al (2005), Song et al (2006) and Byrne et al (2015) that showed an equilibrium near the  
484 surface between advection and pressure gradient, with a negligible contribution of turbulent mixing above fronts.  
485 The former examined a frontal structure with much larger spatial and temporal characteristics scales than the  
486 mesoscale fronts we considered in our study. The latter two correspond to very different climate conditions.  
487 This may explain the discrepancies between their results and ours. Note that O'Neill et al (2010) showed that  
488 both turbulent mixing and pressure gradient are important in the surface budget. Nevertheless, their case study  
489 presented no capping inversion at the top of the PBL, allowing the pressure gradient anomalies to be maximum  
490 near the surface.

491 In the conceptual framework of LN87, Sea Level Pressure (SLP) gradient anomalies are proportional to SST  
492 gradient anomalies (with opposite signs) but can be compensated by the so-called back-pressure effect, related  
493 to air temperature modifications. The pressure anomaly at a height  $Z$  is considered inversely proportional to  
494 the integral of the temperature anomaly between  $Z$  and the top of the PBL. Above warm SST anomalies, the  
495 pressure decrease, due to air warming, is attenuated by the PBL thickening (that induces a pressure increase).  
496 The symmetric occurs for cold SST anomalies. In a situation of air temperature inversion, the back-pressure  
497 effect can be largely strengthened as shown by Hashizume et al (2002) in the EEP. Above warm SST anomalies,  
498 the inversion height ( $Z_0$ ) increase leads to an air temperature decrease (Fig. 14a) and, thus, positive pressure

499 anomalies in the upper part of the PBL. These anomalies compensate the pressure decrease created by air  
 500 warming in the lower PBL leading, overall, to much weaker SLP anomalies than expected in LN87 framework.  
 501 Again, the symmetrical situation is obtained above cold SST anomalies. Note that, according to Small et al  
 502 (2008), this effect requires relatively weak winds so that the SST gradient influence can reach the temperature  
 503 inversion above the frontal zone.

504 The PCS presents a strong temperature inversion near 600 m (Fig. 14b for July 2007). Following Small et al  
 505 (2008), the length scale of the thermal adjustment is  $L_p = \frac{V_1 h^2}{K_T}$ . With  $V_1 \sim 7 \text{ m s}^{-1}$ ,  $h \sim 600 \text{ m}$  and  $K_T \sim 40 \text{ m}^2$   
 506  $\text{s}^{-1}$ ,  $L_p \sim 63 \text{ km}$ , which is smaller than the typical frontal zone length ( $\sim 100 \text{ km}$ ) considered here. This suggests  
 507 that a strong back-pressure effect could exist over mesoscale fronts in the region. To examine this mechanism,  
 508 vertical profiles of temperature anomalies are plotted on Figure 14c<sup>3</sup>. Warm (cold) SST anomalies induce warm  
 509 (cold, respectively) air temperature anomalies below  $Z_0$  and cold (warm) air temperature anomalies above  
 510 (Figure 14c), as described in Hashizume et al (2002). Consequently, SST gradients create downwind pressure  
 511 gradients of the same sign in the upper PBL (Fig. 11a and c). These pressure gradients accelerate (decelerate)  
 512 the wind in the upper layers when it flows above warm to cold (cold to warm, respectively) fronts. Below, their  
 513 intensity decreases, resulting in very little influence of the pressure on the surface flow. Kilpatrick et al (2014)  
 514 also showed that low SLP gradients above SST fronts are due to a back-pressure effect following Hashizume  
 515 et al (2002)'s mechanism.

516 Note that besides their weak influence above fronts, SLP gradient anomalies seem to play an important role  
 517 away from the SST gradient zone, where it acts to equilibrate the turbulent mixing and maintain the wind  
 518 anomalies (not shown). This is consistent with Spall (2007b), nevertheless this analysis is beyond the scope of  
 519 the present study.

---

<sup>3</sup> SST anomalies creates 10 m temperature anomalies that are advected slightly downwind of the SST anomalies (not shown). Thus, the air temperature anomalies vertical profiles (Fig. 14c) are normalized with the 10-m air temperature anomalies values rather the SST values.

## 5.3 About the relation between WS divergence and SST Laplacian

In the present work, we examine the relation between WS and SST mesoscale fields (1) and its two derived relations (5) and (6). However, another relation has been identified by Minobe et al (2008) in the Kuroshio region:

$$\text{div}(\vec{v}_1') \propto \text{div}(\overrightarrow{\text{grad}}(SST')) = \overrightarrow{\nabla}^2(SST') \quad (13)$$

Relation (13) has also been found in idealized simulations with very weak background wind conditions (Lambaerts et al, 2013). In our region, we find correlation associated to (13) much weaker than for relations (1), (5) and (6) (not shown).

While several mechanisms have been invoked to relation (1), Minobe et al (2008) proposed a mechanism to explain (13) based only on pressure anomalies. Following LN87, they consider the vertically averaged momentum balance in the PBL, approximating the PBL wind velocity and pressure by surface fields and considering the surface pressure anomalies proportional to the SST anomalies. These are strong hypothesis: O'Neill et al (2010) and Kilpatrick et al (2014) showed large differences between PBL-integrated and surface fields. Also, Brachet et al (2012) and Piazza et al (2015) noticed that SLP anomalies are not proportional to SST anomalies but to vertically integrated air temperature anomalies. Thus, a strong back-pressure effect as in our region (Sec.5.2) could lead to a very weak relation between SST and SLP anomalies. Another reason for not finding clear evidence for (13) in our case may be because the focus is on the PBL response to mesoscale structures evolving in time while Minobe et al (2008) used 4 years-averaged fields. Brachet et al (2012) showed indeed different atmospheric responses to the SST when considering long-term mean or 10-day mean fields.

It is important to note that (1) and (13) describe two different relations between SST and WS mesoscale fields but they do not reveal the underlying mechanisms. Indeed, Minobe et al (2008) explains (13) by a process based only on pressure anomalies while (1) is explained by several processes (see Sec. 1), among which pressure anomalies.

## 6 Summary and conclusions

Using satellite observations and a high resolution ocean-atmosphere coupled model, correlated patterns between mesoscale SST and WS intensity in the PCS are evidenced. Spatial and seasonal variations of the coupling strength, measured as the regression between WS intensity and SST anomalies, bear noticeable similarities in model simulations and observations. In particular, there is an important seasonal variability, the mesoscale coupling being much stronger in winter than in summer. Spatial variations seem to be related to large-scale fields such as the surface wind steadiness and mean speed. An in-depth analysis of dynamical processes in the atmospheric PBL shows that the stress increase (decrease) above warm (cold) SST anomalies is primarily due to an enhanced (weakened) turbulent kinetic energy. It is partially counterbalanced by the wind velocity shear decrease (increase) over warm (cold) SST anomalies, associated to vertical mixing. Using a downwind momentum budget, we show that the wind velocity shear anomalies are mainly caused by the momentum turbulent mixing in frontal regions. Pressure gradient anomalies are negligible near the surface in frontal regions because of a back-pressure effect related to air temperature inversion. Comparing austral summer and winter, the WS response is twice as strong in winter as in summer because the large-scale wind shear (larger in winter) makes the action of the turbulent stress more efficient.

The described mechanisms at work in the PCS region may be different in other regions. Indeed the back pressure effect is expected to be much lower in unstable regions without temperature inversion. In addition, as underlined by Spall (2007b), the momentum balance depends on the latitude with stronger Coriolis effect at higher latitude. This could result in stronger wind direction anomalies which may no longer be negligible. Also, as described by Small et al (2008), stonger wind conditions and/or stronger SST gradients could modify the equilibrium above frontal regions, as the air column has less time to adjust to the SST changes before being advected. Finally, the coupling mechanisms may depend on the size of the mesoscale structures (Byrne et al, 2015) that can vary geographically.

In this study we focus on the PBL response to SST anomalies in the PCS. The impact of mesoscale SST-induced WS intensity anomalies on the ocean dynamics is not addressed. Mesoscale surface currents also alter

567 surface wind by friction (see Sec. 2.2.1). WS intensity and WS curl anomalies, generated through these effects,  
568 can largely impact ocean eddies (e.g. Jin et al, 2009) and Ekman pumping intensity (Gaube et al, 2015).  
569 Mesoscale air-sea coupling may also induces a thermal damping of eddies (Shuckburgh et al, 2010; Kirtman  
570 et al, 2012). In the PCS, and more generally in EBUS, the ocean mesoscale eddy activity plays an important  
571 role in the system functioning. Eddy advection is an important part of heat and momentum balance (e.g. Colas  
572 et al, 2012, 2013). Eddies are also important for the ecosystem as they drive a spatial redistribution of the  
573 upwelled nutrients and planktons (e.g. Lathuilière et al, 2010; Bertrand et al, 2014). Thus, ocean-atmosphere  
574 interactions at mesoscale may have a role on the dynamics and biological activity in EBUS and its importance  
575 is still to be fully elucidated.

576 **Acknowledgements** This work is part of V. Oerder's PhD thesis, sponsored by the Ministère de l'Enseignement Supérieur  
577 et de la Recherche. It is also part of the ANR project "PULSATION-11-MONU-010" and the LEFE/GMMC project "NEM-  
578 PECH". Simulations were performed on the supercomputer Curie from the GENCI at the CEA (projects 2011040542, 2012061047  
579 and 2014102286). The authors want to thank Françoise Pinsard and Eric Maisonnave for their help in setting-up the coupled  
580 model NEMO-OASIS-WRF and Guillaume Samson, Hervé Giordani and Patrick Marchesiello for useful discussions. F. Lemarié  
581 acknowledges the support of the French LEFE/GMMC program through project SIMBAD QSCAT WS data were provided by  
582 the CERSAT and are available online at <ftp://ftp.ifremer.fr/ifremer/cersat/products/gridded/mwf-quikscat/data/>. Microwave OI  
583 SST data are produced by Remote Sensing Systems and sponsored by National Oceanographic Partnership Program (NOPP),  
584 the NASA Earth Science Physical Oceanography Program, and the NASA MEaSUREs DISCOVER Project. Data are available at  
585 [www.remss.com](http://www.remss.com). Shortwave radiation from the ISCCP are available in the Objectively Analyzed air-sea Fluxes data and can be  
586 downloaded at <http://oafux.whoi.edu/>. VOCALS-REx wind data are available online at <ftp://precip.meas.ncsu.edu/pub/vocals/>.  
587 Numerical data were obtained by model experiments described in Sec. 2. Contact the corresponding author for more information  
588 ([vera.oerder@locean-ipsl.upmc.fr](mailto:vera.oerder@locean-ipsl.upmc.fr)).

589 **Appendix : Double time averaging of the momentum balance**

590 The mechanisms driving the feedback of the SST anomalies on the wind speed are investigated. Monthly mean  
 591 wind speed anomalies  $\langle V \rangle'$ , proportional to the monthly mean SST anomalies  $\langle SST \rangle'$ , are observed in our  
 592 simulation (with primes marking the mesoscale anomalies and  $\langle \rangle$  the temporal average). We want to identify  
 593 the dominant mechanism that creates  $\langle V \rangle'$ . In this appendix, we explain why a simple time averaging of a  
 594 momentum balance does not explain the mean wind speed. Then we present the double time averaging that  
 595 should be used. It is similar to the one included in the NEMO code (Madec, 2008).

596 A simple time-average of 1D momentum balance:

$$\partial_t V = \sum_{F_n \in \{Forces\}} F_n \quad (14)$$

597 relates the forcing time average to the difference between the final and initial wind speed but not to the average  
 598 wind speed  $\langle V \rangle$ , which is the variable of interest :

$$\sum_{F_n \in \{Forces\}} \langle F_n \rangle = \langle \partial_t V \rangle = \left\langle \frac{\Delta V}{\Delta t} \right\rangle = \frac{V(0) - V(N_{step})}{\Delta t} \quad (15)$$

599 with  $V(p)$ , the wind speed  $p$  time steps after the beginning of the month,  $N_{step}$  the number of time steps during  
 600 July,  $\Delta t$  the time step duration, and  $\Delta V = V(p) - V(p-1)$  the wind speed difference between 2 time steps.

The monthly mean wind speed is  $\langle V \rangle = \frac{1}{N_{step}+1} \sum_{p=0}^{N_{step}} V(p)$  and  $V(p)$  can be expressed using the initial conditions  $V(0)$  :  $V(p) = V(0) + \sum_{k=1}^p \Delta V$ , so, we obtain :

$$\begin{aligned} \langle V \rangle &= \frac{1}{N_{step}+1} \sum_{p=0}^{N_{step}} \left( V(0) + \sum_{k=1}^p \Delta V \right) \\ &= V(0) + \frac{1}{N_{step}+1} \sum_{p=0}^{N_{step}} \left( \sum_{k=1}^p \Delta V \right) \end{aligned} \quad (16)$$

601 We introduce a new metric  $[F]$ , the double time averaging of a quantity  $F$ , defined as :

$$[F] = \frac{1}{N_{step} + 1} \sum_{p=0}^{N_{step}} \left( \sum_{k=1}^p F \right) \quad (17)$$

602 (16) can be written  $\langle V \rangle = V(0) + [\Delta V]$ , *i.e.*

$$\frac{\langle V \rangle - V(0)}{\Delta t} = \left[ \frac{\Delta V}{\Delta t} \right] \quad (18)$$

603  $[ \ ]$  is a linear operator, so, using (14), we obtain :

$$\frac{\langle V \rangle - V(0)}{\Delta t} = \left[ \frac{\Delta V}{\Delta t} \right] = [\partial_t V] = \sum_{F_n \in \{Forces\}} [F'_n] \quad (19)$$

604 The left-hand side represents the mean temporal variation around the initial state  $V(0)$ . The relative contribution  
605 of  $[F'_n]$  indicates the dominant mechanisms.

**References**

- 607 Adcroft A, Hill C, Marshall J (1997) Representation of topography by shaved cells in a height coordinate ocean  
608 model. *Mon Wea Rev* 125:2293 – 2315, doi: 10.1175/1520-0493(1997)125<2293:ROTBSO>2.0.CO;2
- 609 Benshila R, Durand F, Masson S, Bourdallé-Badie R, de Boyer Montégut C, Papa F, Madec G (2014)  
610 The upper bay of Bengal salinity structure in a high-resolution model. *Ocean Model* 74:36–52, doi :  
611 10.1016/j.ocemod.2013.12.001
- 612 Bertrand A, Grados D, Colas F, Bertrand S, Capet X, Chaigneau A, Vargas G, Mousseigne A, Fablet R (2014)  
613 Broad impacts of fine-scale dynamics on seascape structure from zooplankton to seabirds. *Nat Commun*  
614 5:5239, doi : 10.1038/ncomms6239
- 615 Blanke B, Delecluse P (1993) Variability of the Tropical Atlantic ocean simulated by a general circula-  
616 tion model with two different mixed layer physics. *J Phys Oceanogr* 23:1363–1388, doi : 10.1175/1520-  
617 0485(1993)023<1363:VOTTAO>2.0.CO;2
- 618 Boe J, Hall A, Colas F, McWilliams J, Qu X, Kurian J, Kapnick S (2011) What shapes mesoscale wind anomalies  
619 in coastal upwelling zones ? *Clim Dyn* 36:2037–2049, doi : 10.1007/s00382-011-1058-5
- 620 Bourras D, Reverdin G, Giordani H, Caniaux G (2004) Response of the atmospheric boundary layer to a  
621 mesoscale oceanic eddy in the northeast atlantic. *J Geophys Res* 109:D18,114, doi : 10.1029/2004JD004799
- 622 Brachet S, Codron F, Feliks Y, Ghil M, Treut HL, Simonnet E (2012) Atmospheric circulations induced by a  
623 midlatitude SST front: A GCM study. *J Clim* 25:1847–1853, doi : 10.1175/JCLI-D-11-00329.1
- 624 Bryan FO, Tomas R, Dennis JM, Chelton DB, Loeb NG, McClean JL (2010) Frontal scale air–sea interaction  
625 in high-resolution coupled climate models. *J Clim* 23:6277–6291, doi : 10.1175/2010JCLI3665.1
- 626 Businger J, Shaw W (1984) The response of the marine boundary layer to mesoscale variations in sea-surface  
627 temperature. *Dyn Atmos Oceans* 8:267–281, doi : 10.1016/0377-0265(84)90012-5
- 628 Byrne D, Papritz L, Frenger I, Münnich M, Gruber N (2015) Atmospheric response to mesoscale sea surface  
629 temperature anomalies: Assessment of mechanisms and coupling strength in a high-resolution coupled model  
630 over the South Atlantic. *J Atmos Sci* 72:1872–1890, doi : 10.1175/JAS-D-14-0195.1

- 631 Capet X, Colas F, Penven P, Marchesiello P, McWilliams J (2008) Eddies in eastern-boundary subtropical  
632 upwelling systems. *AGU Monograph* 177:131–147, doi : 10.1029/177GM10
- 633 Castelao R (2012) Sea surface temperature and wind stress curl variability near a cape. *J Phys Oceanogr*  
634 42:2073–2087, doi : 10.1175/JPO-D-11-0224.1
- 635 CERSAT (2002) Mean wind fields (MWF product)-user manual-volume1: Quikscat. C2-MUT-W-04-IF.  
636 CERSAT-IFREMER [Http://www.ifremer/cersat.fr](http://www.ifremer/cersat.fr)
- 637 Chelton DB, Esbensen SK, Schlax MG, Thum N, Freilich MH, Wentz FJ, Gentemann CL, McPhaden MJ,  
638 Schopf PS (2001) Observations of coupling between surface wind stress and sea surface temperature in the  
639 Eastern Tropical Pacific. *J Clim* 14:1479–1498, doi : 10.1175/1520-0442(2001)014<1479:OOCBSW>2.0.CO;2
- 640 Chelton DB, Schlax MG, Freilich MH, Milliff RF (2004) Satellite measurements reveal persistent small-scale  
641 features in ocean winds. *Science* 303:978–983, doi : 10.1126/science.1091901
- 642 Chelton DB, Schlax MG, Samelson RM (2007) Summertime coupling between sea surface temperature and wind  
643 stress in the California Current System. *J Phys Oceanogr* 37:495–517, doi : 10.1175/JPO3025.1
- 644 Chen F, Dudhia J (2001) Coupling an advanced land surface–hydrology model with the penn state–NCAR MM5  
645 modeling system. part ii: Preliminary model validation. *Mon Weather Rev* 129(4):587–604, doi : 10.1175/1520-  
646 0493(2001)129<0587:CAALSH>2.0.CO;2
- 647 Chou M, Suarez MJ (1994) An efficient thermal infrared radiation parameterization for use in general circulation  
648 models. NASA Tech Memo p 84
- 649 Colas F, McWilliams JC, Capet X, Kurian J (2012) Heat balance and eddies in the Peru-Chile current system.  
650 *Clim Dyn* 39(1-2):509–529, DOI 10.1007/s00382-011-1170-6
- 651 Colas F, Capet X, McWilliams JC, Li Z (2013) Mesoscale eddy buoyancy flux and eddy-induced circulation in  
652 Eastern Boundary Currents. *J Phys Oceanogr* 43:1073–1095, doi : 10.1175/JPO-D-11-0241.1
- 653 Davey M, et al (2002) STOIC: a study of coupled model climatology and variability in tropical ocean regions.  
654 *Clim Dyn* 18(5):403–420, doi 10.1007/s00382-001-0188-6
- 655 Dawe JT, Thompson L (2006) Effect of ocean surface currents on wind stress, heat flux, and wind power input  
656 to the ocean. *Geophys Res Lett* 33:L09,604, doi : 10.1029/2006GL025784

- 657 De Szoeke SP, Fairall CW, Wolfe DE, Bariteau L, Zuidema P (2010) Surface flux observations in the Southeastern  
658 Tropical Pacific and attribution of SST errors in coupled ocean-atmosphere models. *J Clim* 23:4152–4174, doi  
659 : 10.1175/2010JCLI3411.1
- 660 De Szoeke SP, Yuter S, Mechem D, Fairall CW, Burleyson CD, Zuidema P (2012) Observations of stratocumulus  
661 clouds and their effect on the Eastern Pacific surface heat budget along 20°s. *J Clim* 25:8542–8567, doi :  
662 10.1175/jcli-d-11-00618.1.
- 663 Dee DP, et al (2011) The ERA-interim reanalysis: configuration and performance of the data assimilation system.  
664 *Q J R Meteorol Soc* 137:553–597, doi : 10.1002/qj.828
- 665 Desbiolles F, Blanke B, Bentamy A (2014) Short-term upwelling events at the Western African coast related to  
666 synoptic atmospheric structures as derived from satellite observations. *J Geophys Res Oceans* 119:461–483,  
667 doi : 10.1002/2013JC009278
- 668 Dunbar R, Lungu T, Weiss B, Stiles B, Huddleston J, Callahan P, Shirtliffe G, Perry K, Hsu C, Mears C, Wentz  
669 F, Smith D (2006) QuikSCAT science data product user manual, version 3.0. JPL Document D-18053 - Rev  
670 A Jet Propulsion Laboratory, Pasadena, CA
- 671 Dussin R, Treguier AM, Molines JM, Barnier B, Penduff T, Brodeau L, Madec G (2009) Definition of the  
672 interannual experiment ORCA025-B83, 1958-2007. Tech. rep., LPO-09-02
- 673 Farrow DE, Stevens DP (1995) A new tracer advection scheme for Bryan and Cox type ocean general circulation  
674 models. *J Phys Oceanogr* 25:1731–1741, doi : 10.1175/1520-0485(1995)025<1731:ANTASF>2.0.CO;2
- 675 Frenger I, Gruber N, Knutti R, Münnich M (2013) Imprint of Southern Ocean eddies on winds, clouds and  
676 rainfall. *Nat Geosci* 6:608–612, doi : 10.1038/ngeo1863
- 677 Gaube P, Chelton DB, Samelson RM, Schlax MG, O’Neill LW (2015) Satellite observations of mesoscale eddy-  
678 induced Ekman pumping. *J Phys Oceanogr* 45:104–132, doi : 10.1175/JPO-D-14-0032.1
- 679 Giordani H, Planton S, Benech B, Kwon BH (1998) Atmospheric boundary layer response to sea surface tempera-  
680 tures during the SEMAPHORE experiment. *J Geophys Res* 103(C11):25,047–25,060, doi : 10.1029/98JC00892
- 681 Gruber N, Lachkar Z, Frenzel H, Marchesiello P, Münnich M, McWilliams JC, Nagai T, Plattner GK (2011)  
682 Eddy-induced reduction of biological production in Eastern Boundary Upwelling Systems. *Nat Geosci*

- 683 4:787–792, doi : 10.1038/ngeo1273
- 684 Hashizume H, Xie SP, Fujiwara M, Tanimoto TWY (2002) Direct observations of atmospheric boundary layer  
685 response to SST variations associated with tropical instability waves over the Eastern Equatorial Pacific. *J*  
686 *Clim* 15:3379–3393, doi : 10.1175/1520-0442(2002)015<3379:DOOABL>2.0.CO;2
- 687 Hayes S, McPhaden M, Wallace J (1989) The influence of sea surface temperature on surface wind in  
688 the Eastern Equatorial Pacific: weekly to monthly variability. *J Clim* 2:1500–1506, doi : 10.1175/1520-  
689 0442(1989)002<1500:TIOSST>2.0.CO;2
- 690 Hogg A, Dewar WK, Berloff P, Kravtsov S, Hutchinson DK (2009) The effects of mesoscale ocean–atmosphere  
691 coupling on the large-scale ocean circulation. *J Clim* 22:4066–408, doi : 10.1175/2009JCLI2629.1
- 692 Hong S, Lim J (2006) The WRF single-moment 6-class microphysics scheme (WSM6). *J Korean Meteorol Soc*  
693 42(2):129–151
- 694 Hong S, Yign N, Jimy D (2006) A new vertical diffusion package with an explicit treatment of entrainment  
695 processes. *Mon Wea Rev* 134:2318–2341, doi : 10.1175/MWR3199.1
- 696 Hong SY, Pan HL (1996) Nonlocal boundary layer vertical diffusion in a medium-range forecast model. *Mon*  
697 *Wea Rev* 124:2322–2339, doi : 10.1175/1520-0493(1996)124<2322:NBLVDI>2.0.CO;2
- 698 Hu XM, J W NG, F Z (2010) Evaluation of three planetary boundary layer schemes in the WRF model. *J Appl*  
699 *Meteor Climatol* 49:1831–1844, doi : 10.1175/2010JAMC2432.1
- 700 Janjic ZI (1994) The step–mountain eta coordinate model: Further developments of the convection,  
701 viscous sublayer, and turbulence closure schemes. *Mon Wea Rev* 122:927–945, doi : 10.1175/1520-  
702 0493(1994)122<0927:TSMECM>2.0.CO;2
- 703 Jin X, Dong C, Kurian J, McWilliams JC, Chelton DB, Li Z (2009) SST–wind interaction in coastal upwelling:  
704 Oceanic simulation with empirical coupling. *J Phys Oceanogr* 39:2957–2970, doi : 10.1175/2009JPO4205.1
- 705 Jouanno J, Sheinbaum J (2013) Heat balance and eddies in the Caribbean upwelling system. *J Phys Oceanogr*  
706 43:1004–1014, doi : 10.1175/JPO-D-12-0140.1
- 707 Kilpatrick T, Schneider N, Qiu B (2014) Boundary layer convergence induced by strong winds across a midlat-  
708 itude SST front. *J Clim* 27:1698–1718, doi : 10.1175/JCLI-D-13-00101.1

- 709 Kirtman BP, et al (2012) Impact of ocean model resolution on CCSM climate simulations. *Clim Dyn*  
710 39:1303–1328, doi : 10.1007/s00382-012-1500-3
- 711 Koseki S, Watanabe M (2010) Atmospheric boundary layer response to mesoscale SST anomalies in the Kuroshio  
712 extension. *J Clim* 23:2492–2507, doi : 10.1175/2009JCLI2915.1
- 713 Lambaerts J, Lapeyre G, Plougonven R, Klein P (2013) Atmospheric response to sea surface temperature  
714 mesoscale structures. *J Geophys Res Atmos* 118:9611–9621, doi : 10.1002/jgrd.50769
- 715 Lathuilière C, Echevin V, Lévy M, Madec G (2010) On the role of the mesoscale circulation on an idealized  
716 coastal upwelling ecosystem. *J Geophys Res* 115:C09,018, doi : 10.1029/2009JC005827
- 717 Lemarié F (2015) Numerical modification of atmospheric models to include the feedback of oceanic currents on  
718 air-sea fluxes in ocean-atmosphere coupled models. Technical Report RT-464, INRIA Grenoble - Rhône-Alpes,  
719 <https://hal.inria.fr/hal-01184711/file/RT-464.pdf>
- 720 Lindzen R, Nigam S (1987) On the role of sea surface temperature gradients in forcing low level winds and conver-  
721 gence in the Tropics. *J Atmos Sci* 44:2418–2436, doi : 10.1175/1520-0469(1987)044<2418:OTROSS>2.0.CO;2
- 722 Liu W, Zhang A, Bishop J (1994) Evaporation and solar irradiance as regulators of sea surface temperature in  
723 annual and interannual changes. *J Geophys Res* 99:12,623–12,637, doi : 10.1029/94JC00604
- 724 Lévy M, Estubier A, Madec G (2001) Choice of an advection scheme for biogeochemical models. *Geophys Res*  
725 *Let* 28:3725–3728, doi : 10.1029/2001GL012947
- 726 Ma CC, Mechoso C, Robertson A, Arakawa A (1996) Peruvian stratus clouds and Tropical Pacific circulation:  
727 a coupled ocean–atmosphere (GCM) study. *J Clim* 9:1635–1645, doi : 10.1007/s00382-008-0407-5
- 728 Madec G (2008) NEMO ocean engine. Note du Pole de modélisation, Institut Pierre-Simon Laplace (IPSL)  
729 27:ISSN No 1288–1619
- 730 Maloney ED, Chelton DB (2006) An assessment of the sea surface temperature influence on surface wind stress  
731 in numerical weather prediction and climate models. *J Clim* 19:2743–2762, doi : 10.1175/JCLI3728.1
- 732 Meehl GA, Covey C, McAvaney B, Latif M, Stouffer RJ (2005) Overview of the coupled model intercomparison  
733 project. *Bull Am Meteorol Soc* 86:89–93, doi : 10.1175/BAMS-86-1-89

- 734 Minobe S, Kuwano-Yoshida A, Komori N, Xie SP, Small RJ (2008) Influence of the Gulf Stream on the tropo-  
735 sphere. *Nature* 452:206–209, doi : 10.1038/nature06690
- 736 Mlawer E, Taubman S, Brown P, Iacono M, Clough S (1997) Radiative transfer for inhomogeneous atmo-  
737 sphere: RRTM, a validated correlated-k model for the long-wave. *J Geophys Res* 102:16,663–16,682, doi :  
738 10.1029/97JD00237
- 739 Monin AS, Obukhov AM (1954) Basic laws of turbulent mixing in the atmosphere near the ground. *Tr Inst Teor*  
740 *Geofiz Akad Nauk SSSR* 24:1963–1987
- 741 Nakanishi M, Niino H (2009) Development of an improved turbulence closure model for the atmospheric bound-  
742 ary layer. *J Meteorol Soc Jpn* 87:895–912, doi : 10.2151/jmsj.87.895
- 743 Oerder V, Colas F, Echevin V, Codron F, Tam J, Belmadani A (2015) Peru-Chile upwelling dynamics under  
744 climate change. *J Geophys Res Oceans* 120(2):1152–1172, DOI 10.1002/2014JC010299
- 745 O’Neill L, Chelton D, Esbensen S, Wentz F (2005) High-resolution satellite measurements of the atmospheric  
746 boundary layer response to SST variations along the Agulhas return current. *J Clim* 18:2706–2723, doi :  
747 10.1175/JCLI3415.1
- 748 O’Neill LW, Esbensen S, Thum N, Samelson RM, Chelton DB (2010) Dynamical analysis of the boundary layer  
749 and surface wind responses to mesoscale SST perturbations. *J Clim* 23:559–581, doi : 10.1175/2009JCLI2662.1
- 750 O’Neill LW, Chelton DB, Esbensen SK (2012) Covariability of surface wind and stress responses to sea surface  
751 temperature fronts. *J Clim* 25:5916–5942, doi : 10.1175/JCLI-D-11-00230.1
- 752 Paulson CA (1970) The mathematical representation of wind speed and temperature profiles  
753 in the unstable atmospheric surface layer. *J Appl Meteor* 9:857–861, doi : 10.1175/1520-  
754 0450(1970)009<0857:TMROWS>2.0.CO;2
- 755 Penven P, Echevin V, Pasapera J, Colas F, Tam J (2005) Average circulation, seasonal cycle, and  
756 mesoscale dynamics of the Peru current system: A modeling approach. *J Geophys Res* 110:C10,021, doi :  
757 10.1029/2005JC002945
- 758 Perlin N, Skillingstad ED, Samelson RM, Barbour PL (2007) Numerical simulation of air-sea coupling during  
759 coastal upwelling. *J Phys Oceanogr* 37:2081–2093, doi : 10.1175/JPO3104.1

- 760 Perlin N, de Szoeke SP, Chelton DB, Samelson RM, Skyllingstad ED, O'Neill LW (2014) Modeling the atmo-  
761 spheric boundary layer wind response to mesoscale sea surface temperature perturbations. *Mon Wea Rev*  
762 142:4284–4307, doi : 10.1175/MWR-D-13-00332.1
- 763 Piazza M, Terray L, Boé J, Maisonnave E, Sanchez-Gomez E (2015) Influence of small-scale North Atlantic  
764 sea surface temperature patterns on the marine boundary layer and free troposphere: a study using the  
765 atmospheric ARPEGE model. *Clim Dyn* pp 1–19, DOI 10.1007/s00382-015-2669-z
- 766 Putrasahan DA, Miller A, Seo H (2013) Regional coupled ocean–atmosphere downscaling in the South-  
767 east Pacific: impacts on upwelling, mesoscale air–sea fluxes, and ocean eddies. *Ocean Dynam* 63:463–488,  
768 10.1007/s10236-013-0608-2
- 769 Renault L, Hall A, McWilliams JC (2015) Orographic shaping of US West Coast wind profiles during the  
770 upwelling season. *Clim Dyn* DOI 10.1007/s00382-015-2583-4, doi : 10.1007/s00382-015-2583-4
- 771 Resplandy L, Lévy M, Madec G, Pous S, Aumont O, Kumar D (2011) Contribution of mesoscale processes to  
772 nutrient budgets in the Arabian sea. *J Geophys Res* 116:C11,007, doi : 10.1029/2011JC007006
- 773 Samelson RM, Skyllingstad ED, Chelton DB, Esbensen SK, O'Neill LW, Thum N (2006) On the coupling of  
774 wind stress and sea surface temperature. *J Clim* 19:1557–1566, doi : 10.1175/JCLI3682.1
- 775 Samson G, Masson S, Lengaigne M, Keerthi MG, Vialard J, Pous S, Madec G, Jourdain NC, Jullien S, Menkes  
776 C, Marchesiello P (2014) The NOW regional coupled model: Application to the Tropical Indian ocean climate  
777 and tropical cyclone activity. *J Adv Mod Earth Sys* 6(3):700–722, DOI 10.1002/2014MS000324
- 778 Schiffer R, Rossow W (1983) The international satellite cloud climatology project ISCCP: The first project of  
779 the world climate research programme. *Bull Am Meteorol Soc* 64:779–784
- 780 Shin H, Hong SY (2011) Intercomparison of planetary boundary-layer parametrizations in the WRF model for  
781 a single day from CASES-99. *Bound-Layer Meteor* 139(2):261–281, DOI 10.1007/s10546-010-9583-z
- 782 Shuckburgh E, Maze G, Ferreira D, Marshall J, Jones H, Hill C (2010) Mixed layer lateral eddy fluxes mediated  
783 by air–sea interaction. *J Phys Oceanogr* 41:130–144, dOI : 10.1175/2010JPO4429.1
- 784 Skamarock W, Klemp J (2008) A time-split nonhydrostatic atmospheric model for weather research and fore-  
785 casting applications. *J Comp Phys* 227:3465–3485, doi : 10.1016/j.jcp.2007.01.037

- 786 Skillingstad ED, Vickers D, Mahrt L, Samelson R (2006) Effects of mesoscale sea-surface temperature fronts on  
787 the marine atmospheric boundary layer. *Bound-Layer Meteor* 123:219–237, doi: 10.1007/s10546-006-9127-8
- 788 Small R, deSzoek S, Xie S, O’Neill L, Seo H, Song Q, Cornillon P, Spall M, Minobe S (2008) Air–sea interaction  
789 over ocean fronts and eddies. *Dyn Atmos Oceans* 45:274–319, doi : 10.1016/j.dynatmoce.2008.01.001
- 790 Small RJ, Xie SP, Wang Y, Esbensen SK, Vickers D (2005) Numerical simulation of boundary layer structure  
791 and cross-equatorial flow in the Eastern Pacific. *J Atmos Sci* 62:1812–1830, doi : 10.1175/JAS3433.1
- 792 Song Q, Cornillon P, Hara T (2006) Surface wind response to oceanic fronts. *J Geophys Res* 111:C12,006, doi :  
793 10.1029/2006JC003680
- 794 Spall MA (2007a) Effect of sea surface temperature–wind stress coupling on baroclinic instability in the ocean.  
795 *J Phys Oceanogr* 37:1092–1097, doi : 10.1175/JPO3045.1
- 796 Spall MA (2007b) Midlatitude wind stress–sea surface temperature coupling in the vicinity of oceanic fronts. *J*  
797 *Clim* 20:3785–3801, doi : 10.1175/JCLI4234.1
- 798 Strub P, Mesias J, Montecino V, Ruttlant J, Salinas S (1998) Coastal ocean circulation off western South  
799 America. *The Sea* vol 11, chap 10:29–67
- 800 Sweet W, Fett R, Kerling J, La Violette P (1981) Air–sea interaction effects in the lower tropo-  
801 sphere across the north wall of the Gulf Stream. *Mon Wea Rev* 109:1042–1052, doi : 10.1175/1520-  
802 0493(1981)109<1042:ASIEIT>2.0.CO;2
- 803 Valcke S, Craig T, Coquart L (2013) OASIS3-MCT user guide, OASIS3-MCT 2.0. Tech. rep., CERFACS/CNRS  
804 SUC URA No 1875
- 805 Wai MK, Stage S (1989) Dynamical analysis of marine atmospheric boundary layer structure near the Gulf  
806 Stream oceanic front. *Q J R Meteorol Soc* 115:29–44, doi : 10.1002/qj.49711548503
- 807 Wallace J, Mitchell T, Deser C (1989) The influence of sea surface temperature on surface wind in the  
808 Eastern Equatorial Pacific: seasonal and interannual variability. *J Clim* 2:1492–1499, doi : 10.1175/1520-  
809 0442(1989)002<1492:TIOSST>2.0.CO;2
- 810 Webb D, de Cuevas B, Richmond C (1998) Improved advection schemes for ocean models. *J Atmos Ocean*  
811 *Technol* 15(5):1171–1187, doi : 10.1175/1520-0426(1998)015<1171:IASFOM>2.0.CO;2

- 
- 812 Wood R, et al (2011) The VAMOS ocean-cloud-atmosphere-land study regional experiment (VOCALS-REx):  
813 goals, platforms, and field operations. *Atmos Chem Phys* 11:627–654, doi : 10.5194/acp-11-627-2011
- 814 Wyant MC, et al (2010) The PreVOCA experiment: modeling the lower troposphere in the Southeast Pacific.  
815 *Atmos Chem Phys* 10(10):4757–4774, DOI 10.5194/acp-10-4757-2010
- 816 Xie SP (2004) Satellite observations of cool ocean–atmosphere interaction. *Bull Am Meteorol Soc* 85:195–208,  
817 doi : 10.1175/BAMS-85-2-195
- 818 Zhang YC, Rossow WB, Lacis AA, Oinas V, Mishchenko MI (2004) Fluxes from the surface to top of atmosphere  
819 based on ISCCP and other global data sets: refinements of the radiative transfer model and the input data.  
820 *J Geophys Res* 109:D19,105, doi : 10.1029/2003JD004457

## Tables

		CPLM	CPLM50	Observations	CPLY
Peru	summer	0.62 (0.59)	0.68 (0.61)	0.66 (0.52)	0.82 (0.61)
	winter	1.49 (0.77)	1.53 (0.81)	1.00 (0.59)	1.41 (0.73)
Chile	summer	0.27 (0.27)	0.28 (0.23)	0.26 (0.29)	0.39 (0.13)
	winter	1.13 (0.70)	1.14 (0.72)	0.92 (0.40)	1.22 (0.71)

Table 1: WS-SST mesoscale anomalies Regression Coefficient (RC, in  $10^{-2} \text{ N m}^{-2} \text{ }^{\circ}\text{C}^{-1}$ ) off Peru (red box on Fig. 2) and Chile (blue box) during austral summer and winter. RC are computed using the  $1/12^{\circ}$  resolution coupled simulations (CPLM and CPLY) fields, CPLM fields regridded to a 50 km resolution grid (CPLM50), and 50 km resolution observation fields (QSCAT WS and MW OI SST). Correlations between WS and SST mesoscale anomaly fields are indicated between parenthesis

821

		CPLM	CPLM50	Observations
Peru	summer	0.86 (0.71)	0.98 (0.78)	0.9 (0.57)
	winter	1.45 (0.86)	1.68 (0.91)	1.26 (0.6)
Chile	summer	0.76 (0.64)	0.82 (0.70)	0.66 (0.39)
	winter	1.10 (0.85)	1.30 (0.90)	0.95 (0.46)

Table 2: Same as Table 1 for WS divergence anomalies and downwind gradient of the SST anomalies

		CPLM	CPLM50	Observations
Peru	summer	0.51 (0.38)	0.57 (0.44)	0.60 (0.35)
	winter	1.27 (0.71)	1.35 (0.70)	0.99 (0.46)
Chile	summer	0.61 (0.35)	0.57 (0.28)	0.65 (0.27)
	winter	1.14 (0.72)	1.16 (0.69)	0.87 (0.36)

Table 3: Same as Table 1 for WS curl anomalies and crosswind gradient of the SST anomalies

	January (CPLM)	July (CPLM)	July (CPLY)
$\tau'_{tur}$	0.45	0.70	0.76
$\tau'_a$	1.21	2.01	0.8
$\tau'_b$	-0.85	-1.34	-0.1

Table 4: RC ( $10^{-2} \text{ N m}^{-2} \text{ }^{\circ}\text{C}^{-1}$ ) between SST and  $\tau_{tur}, \tau_a$  and  $\tau_b$  anomalies in January and July 2007 for CPLM and July 2007 for CPLY.  $\tau_{tur}$  is the downwind component of the turbulent stress at 20 m.

## Figures

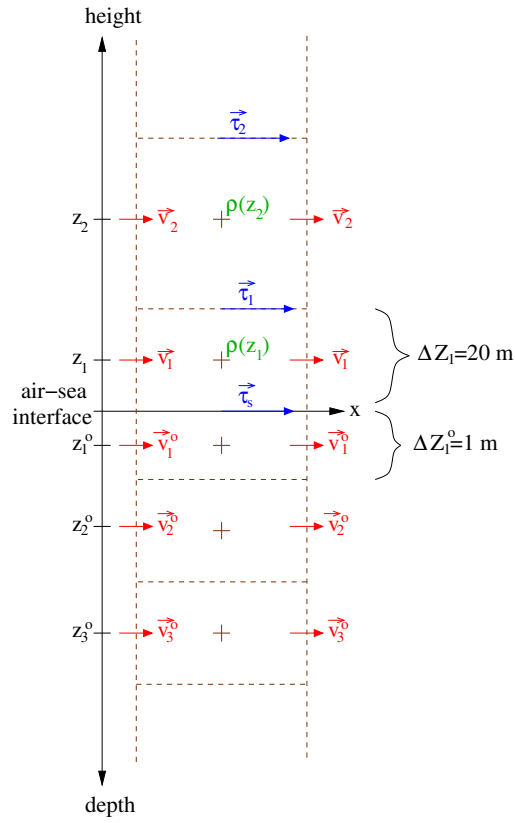


Fig. 1: Vertical structure of the coupled model. Red (blue) vectors represent the model velocities (stress, respectively).  $\Delta Z_1^o$  ( $\Delta Z_1$ ) is the thickness of the first oceanic (atmospheric, respectively) model layer.  $z_N$  ( $z_N^o$ ) is the height of atmospheric (oceanic, respectively) level  $N$ .  $\rho$  is the air density

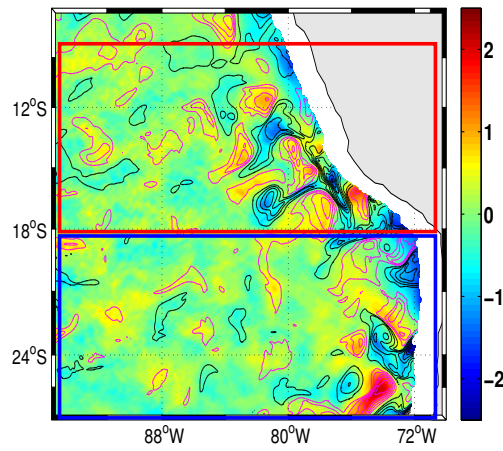


Fig. 2: Surface Wind Stress (WS) mesoscale anomalies (colored,  $10^{-2} \text{ N m}^{-2}$ ). Sea Surface Temperature (SST) anomalies (contours,  $^{\circ}\text{C}$ ): black (magenta) lines indicate negative (positive, respectively) anomalies, contour interval is  $0.25 \text{ }^{\circ}\text{C}$ . Fields are from the CPLM simulation and are time-averaged over July 2007. The 150 km nearshore zone, where the anomalies are dominated by orographic effects, is removed. Anomalies are computed using a gaussian smoothing filter as described in Sec. 2.3.2. Red box indicates the Peru region and the blue box indicates the Chile region

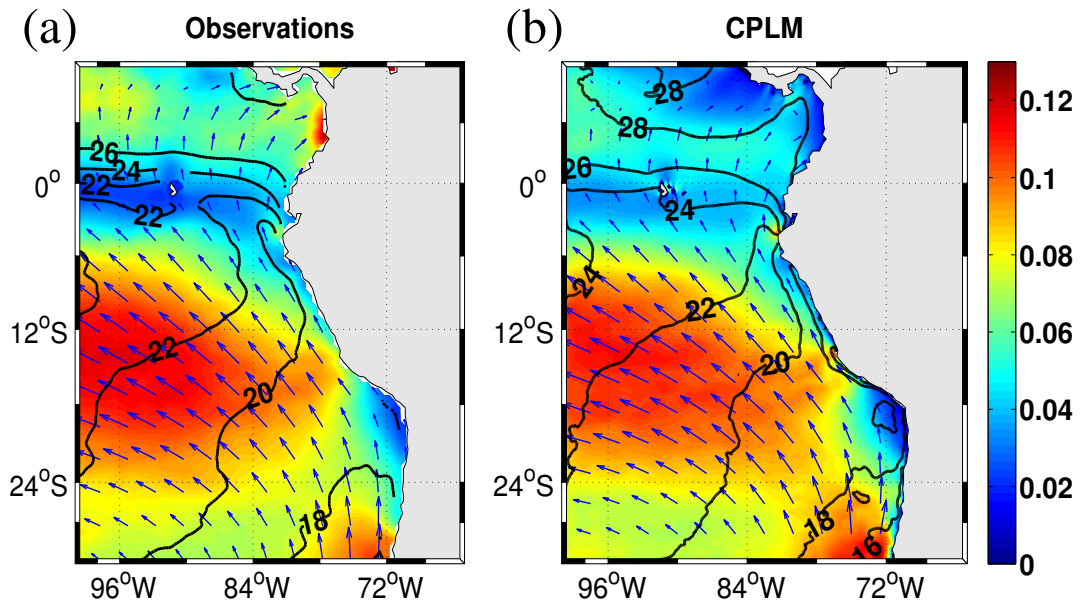


Fig. 3: 2007 annual mean of WS intensity (colored,  $\text{N m}^{-2}$ ), WS direction (blue arrows) and SST (black contours,  $^{\circ}\text{C}$ ). Contour interval is  $2 \text{ }^{\circ}\text{C}$ . (a) Satellite observations and (b) CPLM coupled model simulation

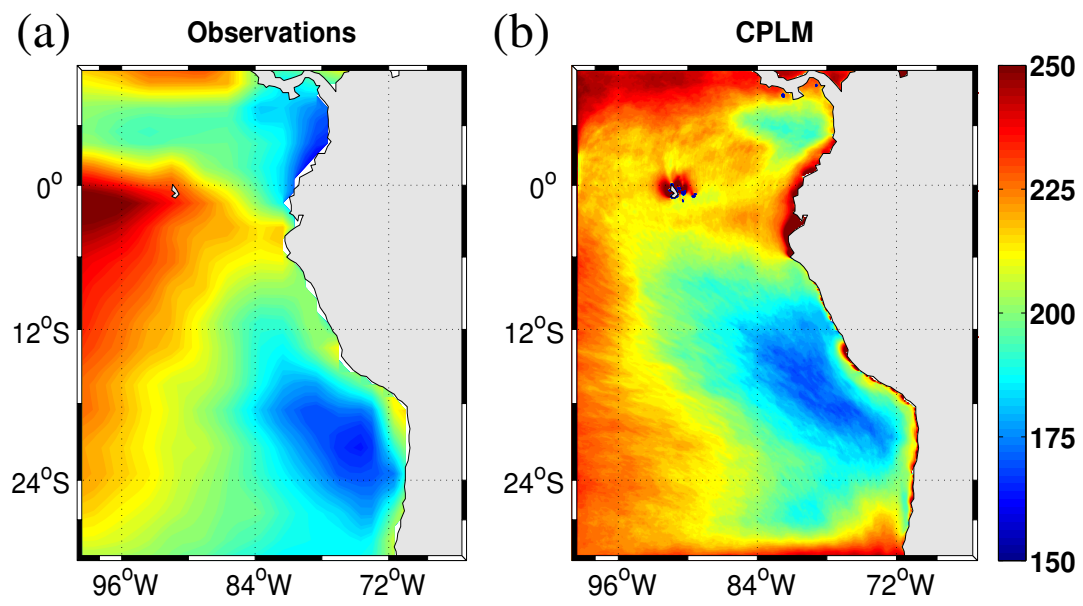


Fig. 4: Short-wave flux at the air-sea interface ( $\text{W m}^{-2}$ , 2007 annual mean). (a) Satellite observations and (b) CPLM simulation.

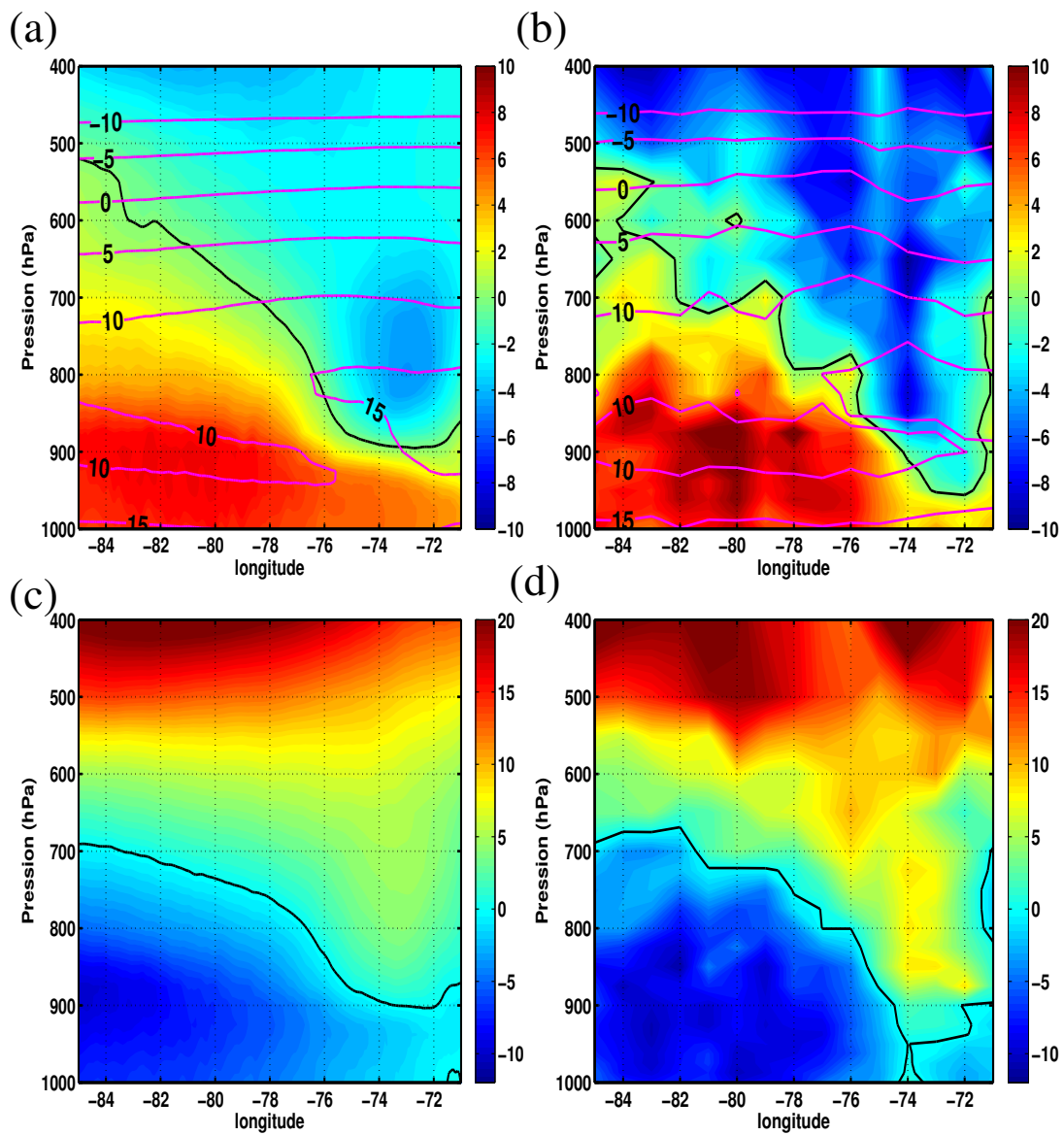


Fig. 5: Zonal sections at 20°S, time-averaged over the period October, 28 to November, 3 2008. (a) CPLM wind meridional velocity (colored,  $\text{m s}^{-1}$ ) and air temperature (contours in magenta,  $^{\circ}\text{C}$ , contour interval is 5  $^{\circ}\text{C}$ ); (b) same as (a) for VOCALS-REx observations; (c) CPLM zonal wind velocity (colored,  $\text{m s}^{-1}$ ); (d) same as (c) for VOCALS-REx observations. Black contours indicate zero velocity.

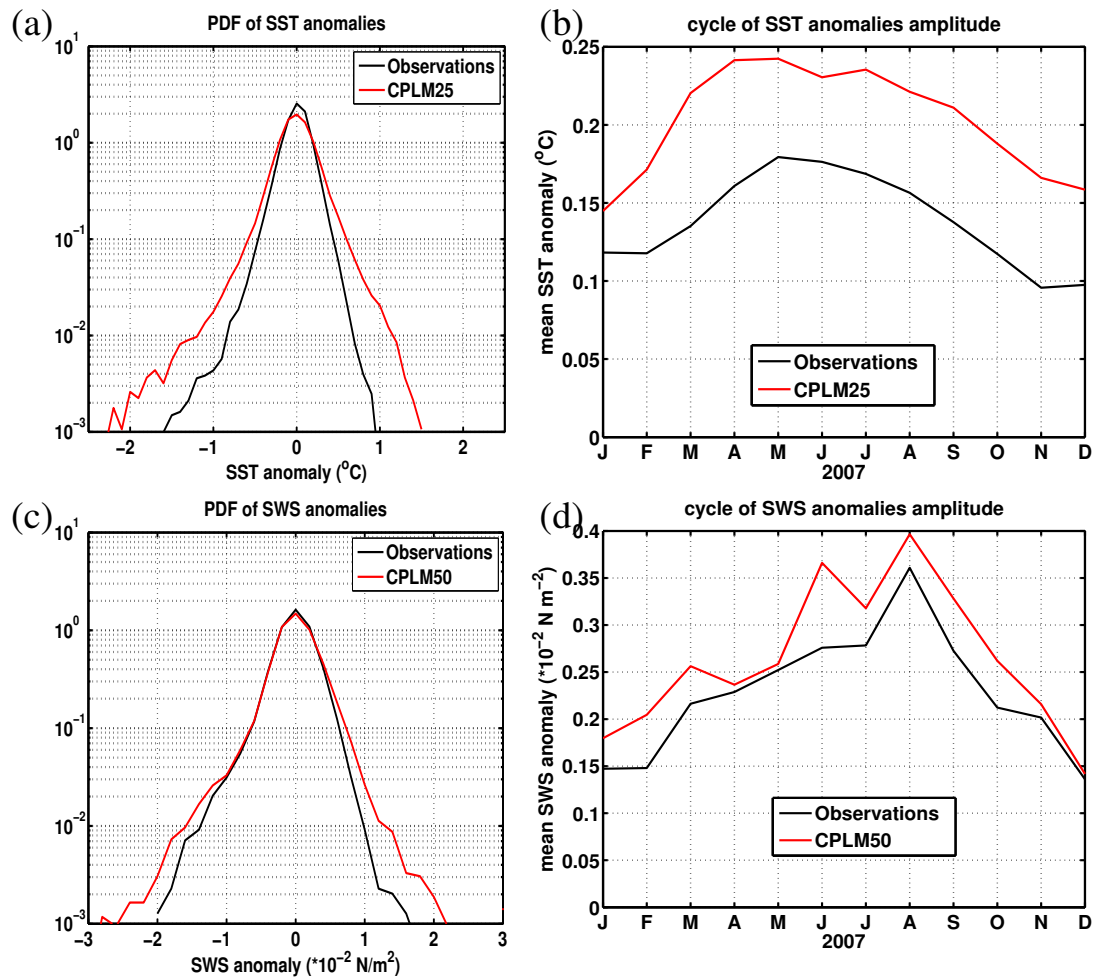


Fig. 6: (a) PDFs of monthly SST anomalies ( $^{\circ}\text{C}$ ) for 2007; (b) Seasonal cycle of the mean SST anomaly absolute value (2007,  $^{\circ}\text{C}$ ); (c) same as (a) for WS anomalies ( $10^{-2} \text{ N m}^{-2}$ ); (d) same as (b) for the mean WS anomaly absolute value ( $10^{-2} \text{ N m}^{-2}$ ). Black line is for observations (MW OI 25 km resolution SST and QSCAT 50 km resolution WS) and red line is for the CPLM simulation. Anomalies are computed over the  $[5^{\circ}\text{S}-27^{\circ}\text{S}]$  domain. CPLM SST and WS fields are regridded to be compared to the observations (Sec. 2.3.1).

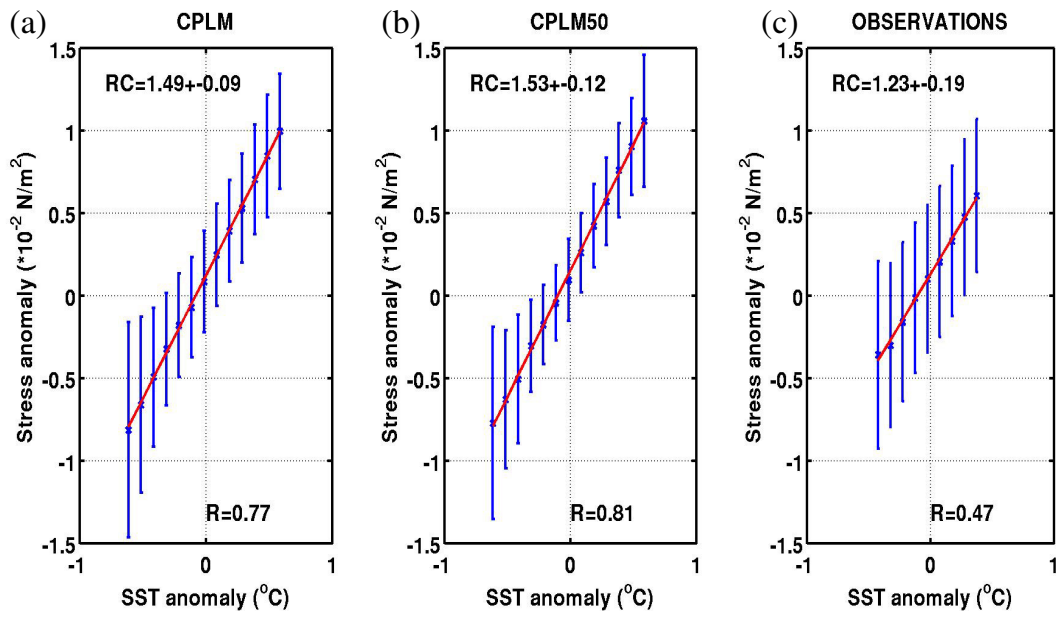


Fig. 7: Binned scatterplot of WS intensity anomalies ( $10^{-2} \text{ N m}^{-2}$ ) with respect to the SST anomalies ( $^{\circ}\text{C}$ ) for (a) CPLM, (b) CPLM50 (CPLM fields regridded at 50 km resolution) and (c) 50 km resolution observed fields (25 km MW OI SST is regridded at 50 km resolution). The binned scatterplots are computed for the Peru region following the methodology described in Sec. 2.3. Correlation (R) and Regression Coefficient (RC, in  $10^{-2} \text{ N m}^{-2} \text{ }^{\circ}\text{C}^{-1}$ ) between SST and WS anomalies are indicated.

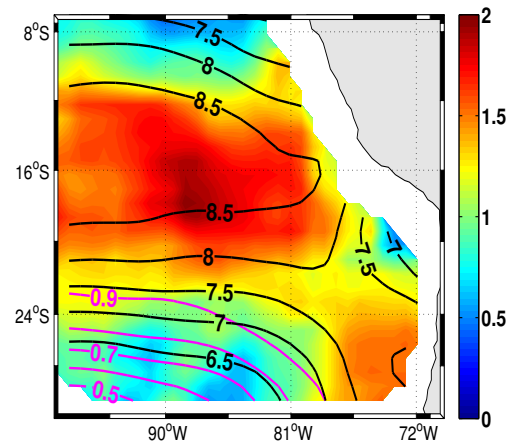


Fig. 8: RC between WS and SST anomalies (colored,  $10^{-2} \text{ N m}^{-2} \text{ }^{\circ}\text{C}^{-1}$ ) in the CPLM simulation for winter 2007. Wind steadiness is indicated by magenta contours with contour interval of 0.1. Wind speed ( $\text{m s}^{-1}$ ) is indicated by black contours, contours interval is  $0.5 \text{ m s}^{-1}$ .

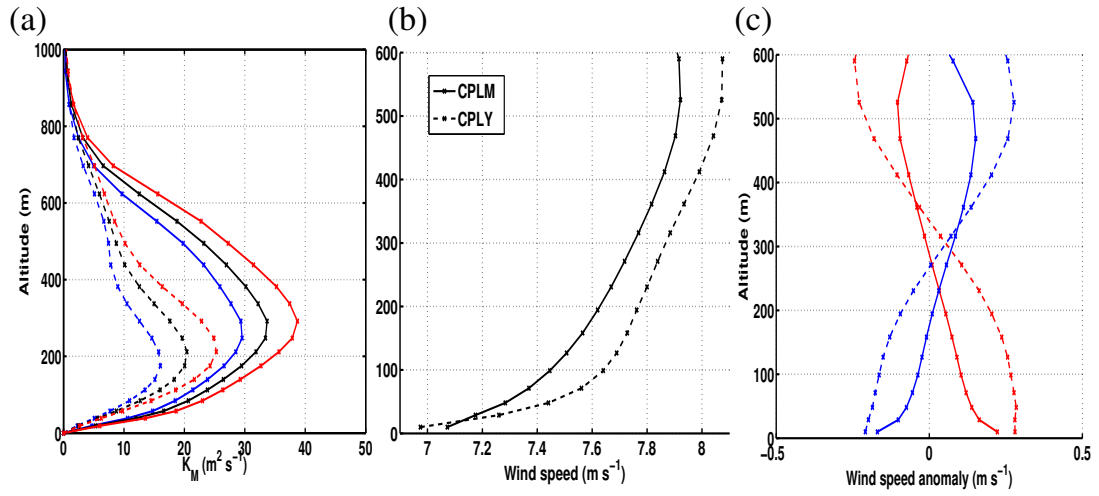


Fig. 9: Vertical profiles computed using time-averaged fields over July 2007 in the Peru region for CPLM (plain lines) and CPLY (dotted lines); (a) mixing coefficient  $K_M$  ( $\text{m}^2 \text{s}^{-1}$ ) mean profile (black), profile above warm SST anomalies (red) and profile above cold SST anomalies (blue). Only anomalies with absolute value larger than  $0.1 \text{ }^\circ\text{C}$  are considered; (b) mean wind speed profile ( $\text{m s}^{-1}$ ). (c) Wind speed anomalies ( $\text{m s}^{-1}$ ) profiles above warm SST anomalies (red) and cold SST anomalies (blue). The vertical axes of the wind speed anomalies were previously rescaled (see Sec. 2.4)

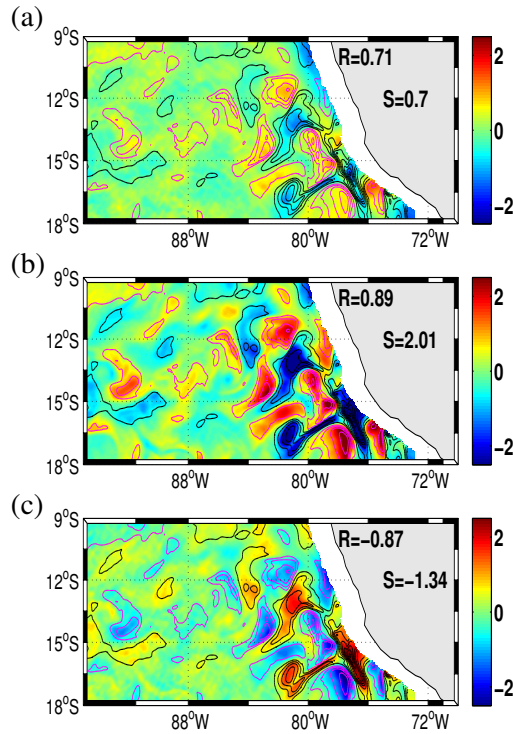


Fig. 10: (a) Downwind turbulent stress anomalies  $\tau'_1$  ( $10^{-2} \text{ N m}^{-2}$ ) at 20 m height.  $\tau'_1$  is decomposed into  $\tau'_a$  and  $\tau'_b$  with  $\tau'_a$  related to the mixing coefficient  $K_M$  anomalies and  $\tau'_b$  proportional to the wind speed shear anomalies; (b)  $\tau'_a$  ( $10^{-2} \text{ N m}^{-2}$ ) at 20 m. (c)  $\tau'_b$  ( $10^{-2} \text{ N m}^{-2}$ ) at 20 m. SST anomalies are indicated by contours (black for negative anomalies, magenta for positive anomalies), contour interval is  $0.25 \text{ }^\circ\text{C}$ . Correlation (R) and Regression Coefficient (RC, in  $10^{-2} \text{ N m}^{-2} \text{ }^\circ\text{C}^{-1}$ ) between SST and stress anomalies are indicated.

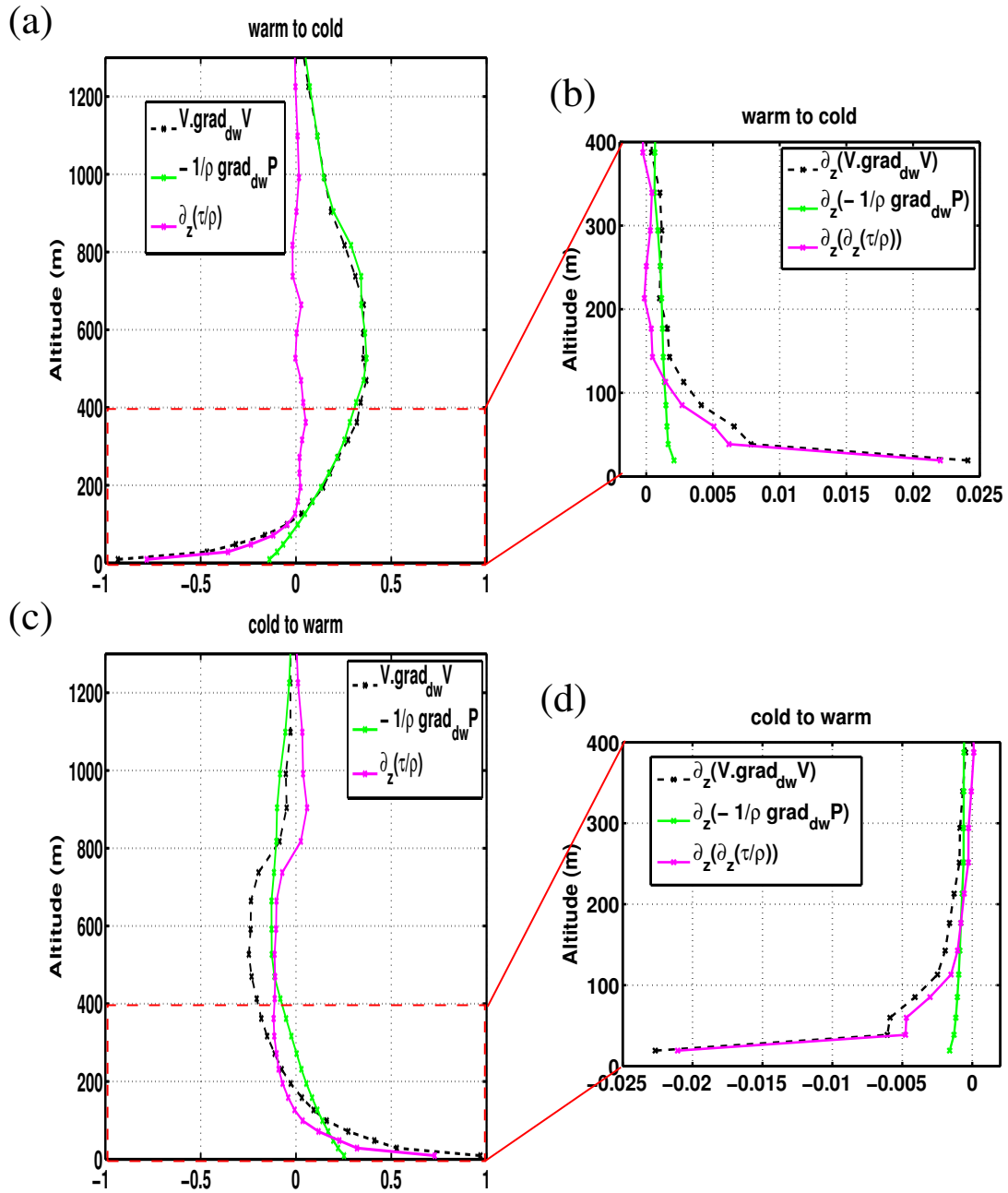


Fig. 11: Composite terms of the downwind momentum balance anomaly above downwind SST gradient anomalies with intensity larger than  $2 \cdot 10^{-5} \text{ }^\circ\text{C m}^{-1}$ . Balance is for July 2007 in CPLM over the Peru region. (a) Composite terms above negative downwind gradient anomalies (warm to cold transition). Downwind momentum balance anomalies (eq. (10)) terms are: Lagrangian acceleration of the air parcel along the streamline (black), momentum turbulent mixing (magenta), pressure term (green), units are  $10^5 \text{ m}^2 \text{ s}^{-2} \text{ }^\circ\text{C}^{-1}$ . Terms have been normalized by the downwind gradient anomalies intensity. (b) vertical shear of the profiles shown in (a), in  $10^5 \text{ m s}^{-2} \text{ }^\circ\text{C}^{-1}$ . (c) same as (a) but for positive downwind gradient anomalies (cold to warm transition). (d) vertical shear of the profile shown in (b)

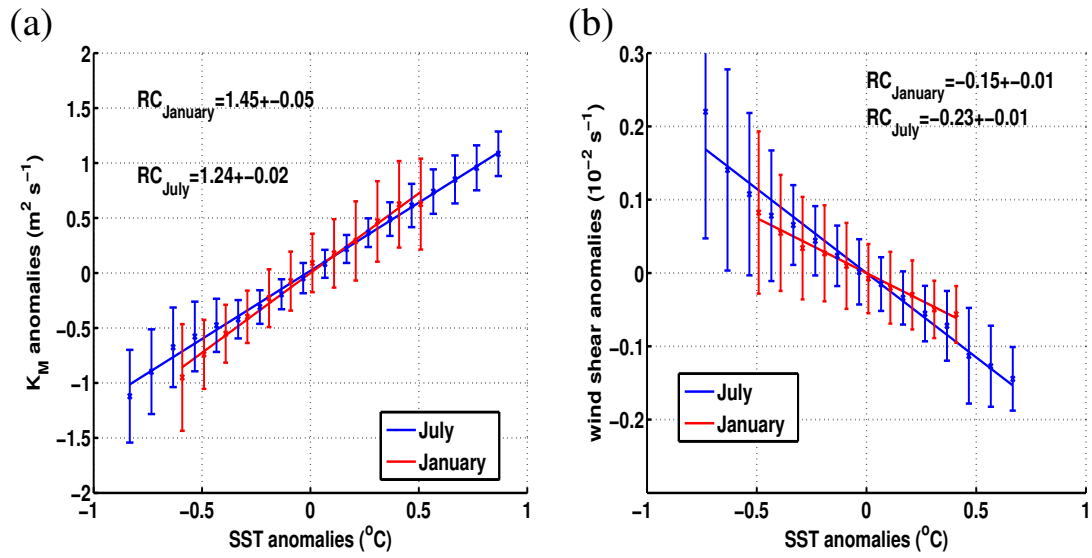


Fig. 12: Binned scatterplot of (a)  $K_M$  ( $\text{m}^2 \text{s}^{-1}$ ) and (b) the intensity of  $\partial_z \vec{v}$  anomalies at 20 m ( $\text{s}^{-1}$ ) with respect to the SST anomalies (°C). Red line is for January and blue line is for July. The RC are also indicated.

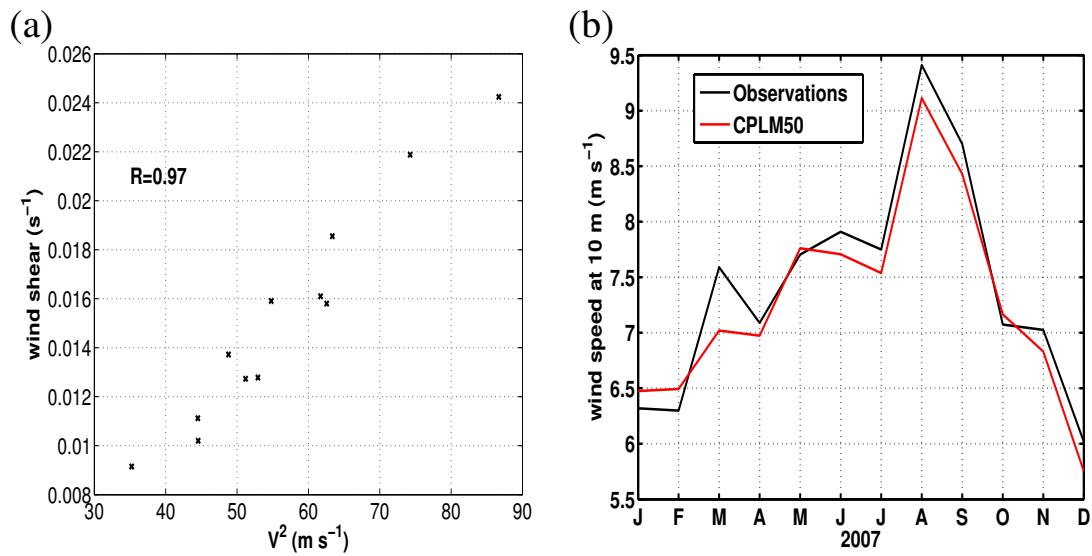


Fig. 13: (a) Scatterplot of the large-scale wind shear  $\|\partial_z \vec{v}\|$  at 20 m with respect to the wind speed at 10 m. Scatterplot values are monthly means spatially averaged over the Peru domain; (b) Seasonal cycle of the wind speed at 10 m, spatially averaged over the Peru domain.

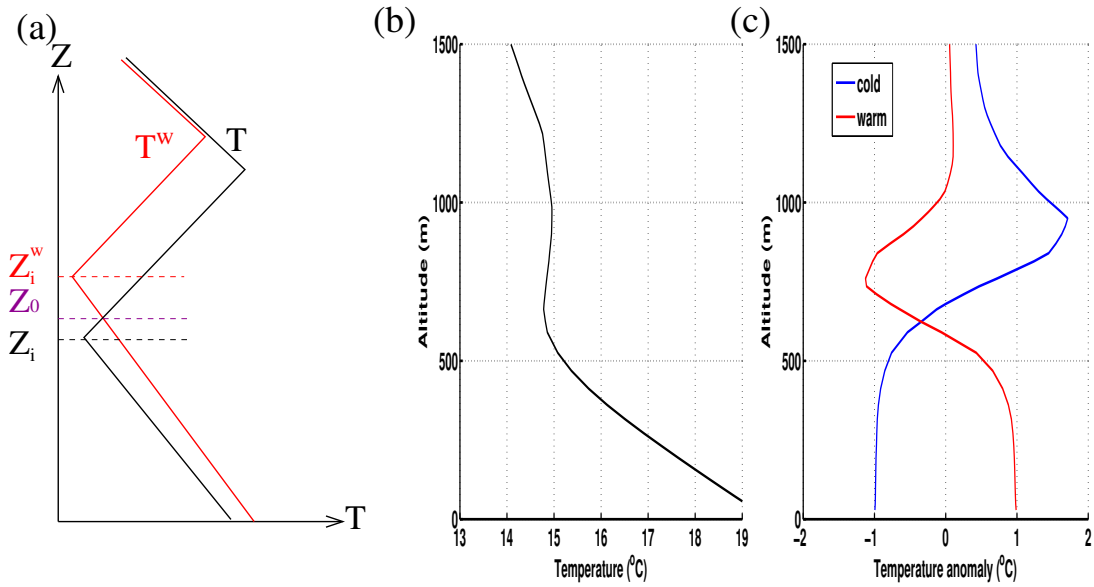


Fig. 14: (a) Scheme of a mean air temperature profile ( $T$ , black line) and the corresponding composites above warm SST anomalies ( $T^w$ , red line) in a region presenting a strong temperature inversion. Inversion height is  $Z_i$  for the  $T$  profile and  $Z_i^w$  for the  $T^w$  profile. Scheme is adapted from Hashizume et al (2002). The symmetric situation occurs for the cold composite (not shown) (b) mean temperature profile ( $^{\circ}\text{C}$ ) over the Peru region during July 2007. (c) Composites of air temperature anomalies above 10 m air temperature warm (red) and cold (blue) anomalies. Only anomalies with an absolute value larger than  $0.5^{\circ}\text{C}$  are considered. Z-axes of each profiles is first normalized (see Sec. 2.4). Profiles are also normalized by the 10 m air temperature anomalies